

1 **Assessing improvements in global ocean pCO₂ machine learning reconstructions with**
2 **Southern Ocean autonomous sampling**

3 Thea H. Heimdal¹, Galen A. McKinley¹, Adrienne J. Sutton², Amanda R. Fay¹, Lucas Gloege³

4 ¹Columbia University and Lamont-Doherty Earth Observatory, Palisades, NY, USA

5 ²Pacific Marine Environmental Laboratory, National Oceanic and Atmospheric Administration,
6 Seattle, WA, USA

7 ³Open Earth Foundation, Marina del Rey, CA, USA

8 *Correspondence to:* Thea H. Heimdal (theimdal@ldeo.columbia.edu)

9

10 **Abstract**

11 The Southern Ocean plays an important role in the exchange of carbon between the atmosphere
12 and oceans, and is a critical region for the ocean uptake of anthropogenic CO₂. However, estimates
13 of the Southern Ocean air-sea CO₂ flux are highly uncertain due to limited data coverage. Increased
14 sampling in winter and across meridional gradients in the Southern Ocean may improve machine
15 learning (ML) reconstructions of global surface ocean pCO₂. Here, we use a Large Ensemble
16 Testbed (LET) of Earth System Models and the pCO₂-Residual reconstruction method to assess
17 improvements in pCO₂ reconstruction fidelity that could be achieved with additional autonomous
18 sampling in the Southern Ocean added to existing Surface Ocean CO₂ Atlas (SOCAT)
19 observations. The LET allows for a robust evaluation of the skill of pCO₂ reconstructions in space
20 and time through comparison to ‘model truth’. With only SOCAT sampling, Southern Ocean and
21 global pCO₂ are overestimated, and thus the ocean carbon sink is underestimated. Incorporating
22 Uncrewed Surface Vehicle (USV) sampling increases the spatial and seasonal coverage of
23 observations within the Southern Ocean, leading to a decrease in the overestimation of pCO₂. A
24 modest number of additional observations in southern hemisphere winter and across meridional
25 gradients in the Southern Ocean, leads to improvement in reconstruction bias and root-mean
26 squared error (RMSE) by as much as 95 % and 16 %, respectively, as compared to SOCAT
27 sampling alone. Lastly, the large decadal variability of air-sea CO₂ fluxes shown by SOCAT-only
28 sampling may be partially attributable to undersampling of the Southern Ocean.

29

Deleted: to

Deleted: ly

Deleted: e

Deleted: ,

Deleted: 6

Deleted: 9

Deleted: using

Deleted: ,

38 **1. Introduction**

39 The ocean plays an important role in mitigating climate change by sequestering anthropogenic
40 carbon emissions. From 1850 to 2023, the oceans have removed a total of 180 ± 35 Gt of carbon
41 (Friedlingstein et al., 2023). In order to fully understand the climate impacts from rising emissions,
42 it is essential to accurately quantify the air-sea CO₂ flux and the global ocean carbon sink in space
43 and time. The Surface Ocean CO₂ Atlas (SOCAT; Bakker et al., 2016) is the largest global
44 database of surface ocean CO₂ observations, with data starting in 1957. The main synthesis and
45 gridded products contain over 33 million high-quality direct shipboard measurements of fCO₂
46 (fugacity of CO₂) with an uncertainty of $< 5 \mu\text{atm}$ (Bakker et al., 2022). However, due to limited
47 resources for ocean observing, limited number of ships/routes, inaccessible regions and unsafe
48 waters, the database covers only about 1% of the global ocean at monthly $1^\circ \times 1^\circ$ spatial resolution
49 over the period of 1982-2023, and is highly biased towards the northern hemisphere.

50 Mapping methods have been developed to estimate full-coverage surface ocean pCO₂
51 across space and time by extrapolating to global coverage from these sparse SOCAT observations
52 (e.g., Landschützer et al., 2014; Rödenbeck et al., 2015; Gloege et al., 2022; Bennington et al.,
53 2022a,b). Most of these data products utilize machine learning (ML) algorithms to estimate a non-
54 linear function between a suite of driver variables (i.e., sea surface temperature - SST, sea surface
55 salinity - SSS, mixed layer depth - MLD, Chlorophyll - Chl-a, xCO₂ - atmospheric CO₂) and
56 surface ocean pCO₂ (the target variable) where these are co-located. The driver variables are
57 proxies for processes influencing ocean pCO₂. Full-coverage driver variable datasets are then
58 processed through these ML algorithms to produce estimated global full-coverage surface ocean
59 pCO₂. Since the data products rely on pCO₂ observations to estimate functions between the target
60 and driver variables, data sparsity remains a fundamental limitation to this technique.

61 It has been suggested that targeted sampling from autonomous platforms combined with
62 ships, filling in the state space of pCO₂, represents a path forward to improve surface ocean pCO₂
63 reconstructions (Bushinsky et al., 2019; Gregor et al., 2019; Gloege et al., 2021; Djeutchouang et
64 al., 2022; Landschützer et al., 2023; Hauck et al., 2023). One major obstacle, however, is that the
65 indirect pCO₂ estimates from floats have high uncertainties ($\pm 11.4 \mu\text{atm}$) and may be biased by
66 as much as $\sim 4 \mu\text{atm}$ (Bakker et al., 2016; Williams et al., 2017; Fay et al., 2018; Gray et al., 2018;
67 Sutton et al., 2021; Mackay and Watson 2021; Wu et al 2022). These large uncertainties and biases

Deleted: against

Deleted: Since

Deleted: 7

Deleted: 2

Deleted: Observation-based data products

Deleted: better constrain

Formatted: Highlight

Deleted: in

Deleted: T

Deleted: ;

Deleted: ;

Deleted: ;

Deleted: ;

Deleted: ;

Deleted: train the algorithms and thus produce these relationships...

Formatted: Subscript

Deleted: likely

Formatted: Font: 12 pt

Formatted: Font: 12 pt

Formatted: Font: 12 pt

84 ~~arise when pCO₂ is not measured directly as in the observations included in SOCAT, but is rather~~
85 ~~estimated using measurements of pH combined with a regression-derived alkalinity estimate~~
86 ~~(Williams et al., 2017; Gray et al., 2018). SOCAT includes only direct pCO₂ observations. Biases~~
87 ~~and uncertainties may have large impacts on global air-sea CO₂ flux estimates, given that the global~~
88 ~~mean air-sea disequilibrium is only 5-8 μatm (McKinley et al., 2020). It is therefore critical that~~
89 ~~bias and uncertainty corrections are well-constrained over different oceanic conditions and over~~
90 ~~time.~~

Formatted: Font: 12 pt

Formatted: Font: 12 pt

Formatted: Font: 12 pt

Formatted: Font: 12 pt, Subscript

Formatted: Font: 12 pt

Deleted: can

91 Uncrewed Surface Vehicles (USVs), such as those manufactured and maintained by
92 Saildrone Inc., represent a new type of autonomous platform that can obtain direct pCO₂
93 observations with significantly lower uncertainties compared to other autonomous methods, and
94 equivalent to the highest-quality shipboard measurements contained in SOCAT (± 2 μatm; Sabine
95 et al., 2020; Sutton et al., 2021). Such improvements in sampling are critically important in the
96 undersampled Southern Ocean. This region is fundamental in terms of the ocean's ability to
97 remove carbon from the atmosphere, being responsible for ~ 40% of the global ocean uptake of
98 anthropogenic CO₂ (Khatriwala et al., 2009). Improved data coverage in the Southern Ocean
99 represents thus a major opportunity to advance our understanding of the global ocean carbon sink
100 (Lenton et al., 2006, 2013; Takahashi et al., 2009; Monteiro et al., 2015; Gregor et al., 2019; Gray
101 et al., 2018; Mongwe et al., 2018; Bushinsky et al., 2019; Sutton et al., 2021; Long et al., 2021;
102 Mackay et al., 2022; Wu et al., 2022; Landschützer et al., 2023; Hauck et al., 2023). A combination
103 of SOCAT and Saildrone USV observations would include ~~high-accuracy data from both the long~~
104 ~~record and global coverage of ship tracks, and the expanded finer resolution of spatial and seasonal~~
105 ~~coverage of the poorly sampled Southern Ocean. Importantly, Saildrone USVs are also able to~~
106 ~~cover the spatial extent and seasonal cycle of the meridional gradients, which has been shown to~~
107 ~~be critical in order to reduce errors in reconstructing surface ocean pCO₂ (Djeutchouang et al.,~~
108 ~~2022). A combined approach, with autonomous samples such as those obtained from Saildrone~~
109 ~~USVs, in addition to high-quality observations collected from ships, represents thus a promising~~
110 ~~solution to improve surface ocean pCO₂ ML reconstructions.~~

Deleted:

111 Here, we assess to what extent surface ocean pCO₂ reconstructions can improve by
112 implementing the pCO₂-Residual machine learning (ML) reconstruction (Bennington et al., 2022a)
113 with the combined inputs of SOCAT and Saildrone USV coverage. However, instead of using ~~real-~~

116 ~~world~~ observations, we sample the target (i.e., surface ocean pCO₂) and driver variables (i.e., SST,
117 SSS, MLD, Chl-a and xCO₂) from our Large Ensemble Testbed (LET) of Earth System Models
118 (ESMs) (e.g., Stamen et al., 2020; Gloege et al., 2021; Bennington et al., 2022a). There are two
119 major benefits of using a testbed compared to actual observations. First, in an ESM, ~~the~~ surface
120 ocean pCO₂ ~~field is~~ ~~provided precisely~~ at all ~~model times and~~ ~~1°x1° points~~. Therefore, the pCO₂
121 reconstructed by the ML algorithm can be robustly evaluated in space and time against a known
122 ‘truth’ (i.e., ‘model truth’). The reconstruction evaluation is thus not limited to the availability of
123 sparse real-world ocean observations. Secondly, a testbed can be used to plan and evaluate the
124 impact of different sampling strategies on the reconstructed pCO₂. It is important to stress that, by
125 using a model testbed, we do not predict real-world surface ocean pCO₂ and air-sea CO₂ fluxes.
126 The goal here is to assess the accuracy with which an ML algorithm can reconstruct the ‘model
127 truth’ given inputs of samples consistent with real-world data coverage from the SOCAT database
128 and Sairdrone USVs.

Deleted: actual

Deleted: known

Deleted: locations

129 By utilizing the observational coverage of SOCAT and Sairdrone USV transects, we assess
130 to what extent the pCO₂-Residual method accurately reconstructs model surface ocean pCO₂ in
131 space and time. ~~We test the impact of two different USV Southern Ocean sampling schemes, the~~
132 ~~first based on a sampling campaign completed in 2019 (Sutton et al., 2021), and the second on~~
133 ~~logistically feasible potential future meridional sampling.~~ Additionally, we explore the timing,
134 magnitude, duration and spatial extent of Southern Ocean USV sample additions that most
135 significantly improve the pCO₂ predictions. ~~Combined, the sampling patterns tested here~~
136 ~~complements previous studies exploring the impact of additional sampling in the Southern Ocean~~
137 ~~based on idealized full global coverage of floats, and float observations from recent deployments,~~
138 ~~including the Southern Ocean Carbon and Climate Observations and Modeling (SOCCOM)~~
139 ~~project, moorings and sailboats (Bushinsky et al., 2019; Denvil-Sommer et al., 2021;~~
140 ~~Djeutchouang et al., 2022; Hauck et al., 2023; Behncke et al., 2024; Landschützer et al., 2023).~~

Formatted: Highlight

Formatted: Highlight

142 2. Methods

143 2.1 The Large Ensemble Testbed (LET)

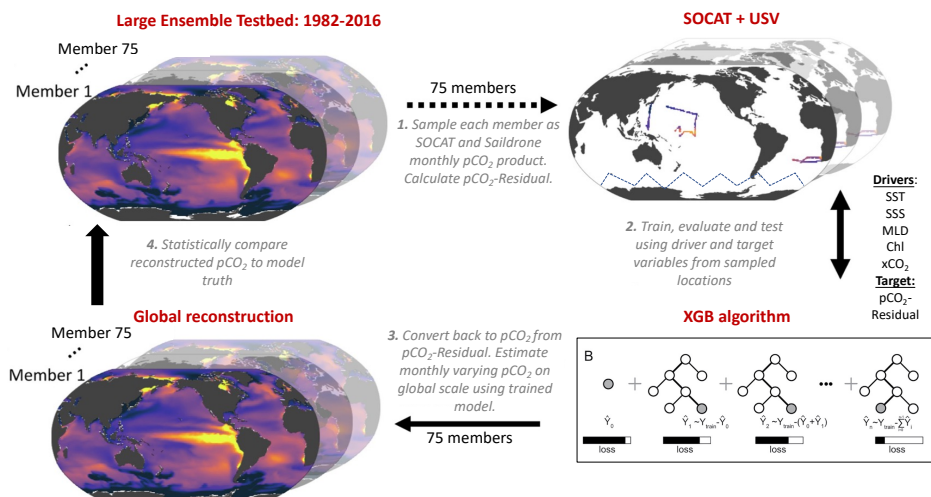
147 In this study, the Large Ensemble Testbed (LET) includes 25 members from three independent
148 initial-condition ensemble models (i.e., CanESM2, CESM-LENS and GFDL-ESM2M; Kay et al.,
149 2015; Rodgers et al., 2015; Fyfe et al., 2017), giving a total of 75 members within the testbed. We
150 do not use the MPI-GE model that was included in the past LET studies because its Southern
151 Ocean pCO₂ seasonality and decadal variability appear to be anomalously large (Gloege et al.,
152 2021; Fay and McKinley, 2021; Bennington et al., 2022a). Each individual Earth System Model
153 (ESM) is an imperfect representation of the actual Earth system, so the multiple Large Ensembles
154 are used to span different model structures and their representation of internal variability. Each
155 ensemble member undergoes the same external forcing (i.e., historical atmospheric CO₂ before
156 2005 and Representative Concentration Pathway 8.5 through 2016, plus solar and volcanic
157 forcing), but the spread across the ensemble members gives a unique trajectory of the ocean-
158 atmosphere state over time, i.e., a different state of internal variability as well as the difference
159 across models.

Deleted: s

160 The LET used in this study includes monthly 1°x1° model output from 1982-2016 (Gloege
161 et al., 2021). For each individual ensemble member of the LET, surface ocean pCO₂ and co-located
162 driver variables (i.e., SST, SSS, Chl-a, MLD, xCO₂) were sampled monthly at a 1°x1° resolution,
163 at times and locations equivalent to SOCAT and Saildrone USV observations (**Fig. 1**; Step 1).
164 While the SOCAT observations were sampled from the testbed matching the actual years of
165 sampling, the USV observations were sampled from the testbed starting in 2007 (for ten-year
166 sampling) or 2012 (for five-year sampling) (see **Sect. 2.4**). As our focus is on reconstruction for
167 the open ocean, testbed output for coastal areas, the Arctic Ocean (>79°N) and marginal seas
168 (Hudson Bay, Caspian Sea, Black Sea, Mediterranean Sea, Baltic Sea, Java Sea, Red Sea and Sea
169 of Okhotsk) were removed prior to algorithm processing.

Deleted: year

170



173
174
175 **Figure 1:** Schematic of the Large Ensemble Testbed (LET; modified from Gloege et al., 2021). **1:** Surface ocean
176 pCO₂ from each of the 75 model members is sampled in space and time mimicking real-world SOCAT and Saildrone
177 USV observations (see Fig. 2; Table 1; Section 2.5). Prior to algorithm processing, pCO₂-Residual is calculated
(Section 2.2). **2:** The pCO₂-Residual (target variable) and co-located driver variables (i.e., SST, SSS, MLD, Chl,
178 xCO₂) sampled from the testbed are processed by the XGBoost (XGB) algorithm (Section 2.3). **3:** Based on the full-
179 coverage of driver variables, pCO₂-Residual is reconstructed globally. This process is repeated 75 times, individually
180 for every single testbed model member. The temperature component (pCO₂-T) is then added back to the pCO₂-
181 Residual for each value. **4:** The globally reconstructed pCO₂ is evaluated against the 'model truth' at all 1°x1° grid
182 cells. SST = sea surface temperature. SSS = sea surface salinity. MLD = mixed layer depth. Chl = chlorophyll. xCO₂
183 = atmospheric concentration of CO₂.

184
185 **2.2 The pCO₂-Residual approach**

186 We used the pCO₂-Residual approach following Bennington et al. (2022a), which removes the
187 well-studied direct effect of temperature on pCO₂ from the LET model output **before** algorithm
188 processing. Temperature has both direct and indirect effects on surface ocean pCO₂. The direct
189 effect of temperature, due to solubility and chemical equilibrium, is that an increase in temperature
190 directly causes an increase in pCO₂ (Takahashi et al., 1993). Indirectly, temperature changes are
191 associated with biological production and wintertime vertical mixing; and these processes tend to
192 result in opposing pCO₂ changes. To build reconstruction algorithms through the data-driven
193 training that occurs in ML, the statistics in all other algorithms developed to date must identify a
194 function that disentangles these competing effects of SST on pCO₂. Here, the algorithm is assisted
195 by removing this known temperature effect, and it must therefore only learn the pCO₂ impacts

Deleted: , i.e., the direct effect of temperature has been removed from the pCO₂ value

Deleted: Since we are using model testbed and not real-world observations, the

Deleted: can

Deleted: be

Deleted: , not just where observations are available

Deleted: ¶

Deleted: prior to

205 from biogeochemical drivers. The pCO₂-Residual method leads to physically understandable
206 connections between the input data and output (Bennington et al., 2022a), which mitigates to some
207 degree ‘black box’ concerns typically associated with ML algorithms (Toms et al., 2020). Further,
208 this method has been shown to perform better against independent observations than other
209 common **mapping methods** (Bennington et al., 2022a). A brief description is provided here, but
210 for further details see Bennington et al. (2022a).

Deleted: **observation-based products**

211 The temperature-driven component of pCO₂ (pCO₂-T) is calculated using this equation:

$$212 \quad p\text{CO}_2\text{-T} = p\text{CO}_2^{\text{mean}} * \exp[0.0423 * (\text{SST} - \text{SST}^{\text{mean}})]$$

213 where pCO₂^{mean} and SST^{mean} is the long-term mean of surface ocean pCO₂ and temperature,
214 respectively, using all 1°x1° grid cells from the testbed. Once pCO₂-T is determined, pCO₂-
215 Residual is calculated as the difference between pCO₂ and the calculated pCO₂-T:

$$216 \quad p\text{CO}_2\text{-Residual} = p\text{CO}_2 - p\text{CO}_2\text{-T}$$

217 Prior to algorithm processing, pCO₂-Residual values > 250 μatm and < -250 μatm from the
218 testbed were filtered out **targeting** values that are not representative of the real ocean. The **majority**
219 **of the** pCO₂-Residual values **that were filtered out** correspond to high pCO₂, above the maximum
220 value in SOCAT (816 μatm; Stamell et al., 2020). The excluded data points (less than 0.2 % per
221 member) mostly occurred in output from the CanESM2 model, and were restricted geographically,
222 predominantly along the western coastline of South America.

Deleted: to

Deleted: se

Deleted: generally

223 The eXtreme Gradient Boosting method (XGB; Chen and Guestrin, 2016) is used to
224 develop an algorithm that allows driver variables (i.e., SST, SSS, Chl-a, MLD, xCO₂) to predict
225 the pCO₂-Residual (**Fig. 1**; Step 2). The pCO₂-Residual and associated feature variables is split
226 into validation, training and testing sets. The test and validation set each account for 20 % of the
227 data, leaving 60 % for training. The validation set is used to optimize the algorithm
228 hyperparameters, which define the architecture of decision trees used in the model. The training
229 set is used to build the decision trees in XGB, while the test set is used to evaluate the performance
230 of the final algorithm. The XGB algorithm for this study used 4,000 decision trees with a maximum
231 depth of 6 levels, **and this was fixed for all experiments**. For the final reconstruction of surface

236 ocean pCO₂ across all space and time points, the previously calculated pCO₂-T values are added
237 back to the reconstructed pCO₂-Residual (Fig. 1; Step 3).

238 The full XGB process, including 1) training/evaluating/testing and 2) reconstructing
239 globally at a monthly resolution, was repeated individually for each LET member. This process
240 provided therefore a total of 75 unique reconstruction vs. ‘model truth’ pairs, which can be
241 statistically compared (Fig. 1; Step 4).

242 2.3 Statistical Analysis in the Testbed

243 The statistical comparisons between the test set and the reconstructions are equivalent to what
244 would be derived using real-world data (‘seen’ values). Here, we calculate error statistics based on
245 the full reconstruction (pCO₂ from all 1°x1° grid cells of the testbed, except for those masked or
246 filtered out). In the full reconstruction, ~99 % of the data do not correspond to SOCAT or
247 Saildrone USV observations used to train the algorithm (Fig. S1). Training data would ideally be
248 removed before performance evaluation, but since the training data represent only ~1 %, the
249 impact of not removing them is negligible (Fig. S2). A suite of statistical metrics can be used to
250 compare the reconstruction to the ‘model truth’ in order to assess how well the algorithm can
251 extrapolate from sparse data to full-field coverage (Fig. 1; Step 4). In this study, we focus on bias
252 and root-mean-squared error (RMSE). Bias is calculated as ‘mean prediction – mean observation’
253 (i.e., pCO₂ predicted by XGB subtracted by the pCO₂ ‘model truth’), and is a measure of over- or
254 underestimation in the reconstructions. RMSE measures the magnitude of the predicted error and
255 is calculated as the square root of the mean of the squared errors. We focus our discussion on the
256 mean across 75 members of the testbed for bias and RMSE. The spread across testbed ensemble
257 members is non-negligible and will be the focus of future work; here, we present the testbed spread
258 primarily in the Supplement.

259 2.4 Overview of sampling patterns and model runs

260 First, we sampled target and driver variables from the LET based on sampling distributions
261 equivalent to that of the SOCAT database (‘SOCAT-baseline’). Then, we combined the ‘SOCAT-
262 baseline’ with testbed output representing additional Saildrone USV coverage in the Southern
263 Ocean. The additional Southern Ocean coverage was based on 1) the Sutton et al. (2021) sampling
264 campaign from 2019 (‘one-latitude’ track) and 2) realistic potential future meridional USV

Formatted: Subscript

Deleted: Since we are using a testbed, we can also include comparisons on additional independent data, referred to as ‘unseen’ values, which represent the 1°x1° grid cells of the ensemble members that

Formatted: Not Highlight

Deleted:

Formatted: Font: Bold

Formatted: Font: Bold

Formatted: Font: Bold

Deleted:

Deleted:

272 observations ('zigzag' track) (see Section 2.4.2; Fig. 2). We performed a total of 10 experimental
273 runs (Table 1). These represent different sampling approaches, including: 1) repeating USV
274 sampling over a five- or ten-year period, 2) varying the number of USVs and thus the total number
275 of monthly 1°x1° observations, and 3) restricting all observations to southern hemisphere winter
276 months. By comparing the different runs, we can assess whether or not certain targeted sampling
277 strategies in the Southern Ocean can improve surface ocean pCO₂ ML reconstructions. As
278 discussed above, the LET runs to 2016 only (Gloege et al., 2021). Saildrone USV observations
279 were therefore sampled from the testbed starting in year 2006 or 2007 (for the ten-year sampling)
280 or 2012 (for the five-year sampling) until 2016, i.e., the final year of the testbed.

281 2.4.1 'One-latitude' runs

282 Six out of the ten experimental runs include the 'one-latitude' track (Table 1). The 2019 Saildrone
283 USV journey (Sutton et al., 2021) covered an 8-month period, from January to August. Since the
284 USV was recovered in early August, it did not cover the entire southern hemisphere winter (Fig.
285 S3). We repeated this 'one-latitude' eight-month sampling pattern for five years ('5Y_J-A'; 2,075
286 observations) and ten years ('10Y_J-A'; 4,150 observations). To evaluate year-round ('YR')
287 coverage, the eight-month sampling period (January-August) was shifted by one month each year
288 for ten years ('10Y_YR'; 4,150 observations). To evaluate the impact of increased sampling, the
289 2019 Saildrone USV track was repeated 12 times with incremental offsets of 1° from the original
290 track, covering an additional 6° north and south (Fig. S4). This 'high-sampling'-run ('x13_10Y_J-
291 A'; 44,250 observations) represents a total of 13 USVs. We also performed an additional 13 USV
292 run, but including observations from southern hemisphere winter ('W') months only
293 ('x13_10Y_W'; 25,395 observations). Finally, considering the cost of deploying 13 USVs, a
294 downscaled 'multiple-USV-winter-only'-run was tested, including five USVs sampling over a
295 period of five years ('x5_5Y_W'; 5,022 observations). This run covers an additional 2° north and
296 south from the original USV track.

297 2.4.2 'Zigzag' runs

298 Four of the ten experimental runs represent realistic potential meridional sampling in the Southern
299 Ocean ('zigzag' tracks; Table 1) as suggested by Djeutchouang et al. (2022). Saildrone USVs can
300 operate at a speed capable of covering the spatial extent of meridional gradients in the Southern

Formatted: Font: Bold

Deleted: 1

Deleted:

Deleted: In order t

Deleted: Furthermore, in order t

Deleted: 2

Formatted: Font: 12 pt, Not Italic

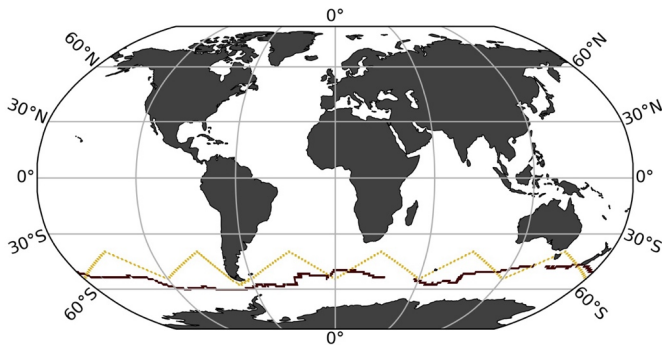
306 Ocean (Djeutchouang et al., 2022). However, Sairdrone USVs are solar powered, and thus their
 307 range is restricted by the availability of solar radiation. To account for this and maintain a realistic
 308 sampling scenario, sampling occurs only to a maximum latitude of 55° S in these experiments.
 309 This alternative sampling pattern represents USVs sailing west to east in a north/south ‘zigzag’
 310 pattern covering 40° S and 55° S for every 30° of longitude (Fig. 2). We created two scenarios.
 311 For the first scenario, every 30° of longitude from 40° S and 55° S is visited every three months
 312 within a single year as suggested by Lenton et al. (2006). Assuming an average Sairdrone USV
 313 speed, this scenario represents four platforms equally spaced around the Southern Ocean. This
 314 sampling pattern was repeated for 10 years, with year-round coverage (‘Zx4_10Y_YR’; 7,600
 315 observations), and for southern hemisphere winter months only (‘Zx4_10Y_W’; 2,500
 316 observations). The second scenario represents a ‘high-sampling’ strategy, where every 30° of
 317 longitude from 40° S and 55° S is visited approximately monthly. This can be achieved by
 318 deploying 10 platforms equally spaced around the Southern Ocean running at an average Sairdrone
 319 USV speed. This sampling pattern is repeated for five years, sampling year-round
 320 (‘Z_x10_5Y_YR’; 11,400 observations) and during southern hemisphere winter months only
 321 (‘Z_x10_5Y_W’; 3,800 observations).

Formatted: Font: 12 pt

Formatted: Font: 12 pt, Not Italic

Deleted: Due to limited solar radiation that powers the Sairdrone USVs, we let the sampling occur at a maximum latitude of 55° S.

Deleted: Considering the



322 **Figure 2:** Sairdrone Uncrewed Surface Vehicle (USV) tracks representing the first circumnavigation around
 323 Antarctica from 2019 in maroon (‘one-latitude’ track; Sutton et al., 2021) and an alternative virtual route with
 324 meridional coverage (‘zigzag’ track).
 325

Run name	SOCAT-baseline	5Y J-A	10Y J-A	10Y YR	x13 10Y J-A	x13 10Y W	x5 5Y W	Z x4 10Y YR	Z x4 10Y W	Z x10 5Y YR	Z x10 5Y W
Saildrone track	NA	One-lat	One-lat	One-lat	One-lat	One-lat	One-lat	Zigzag	Zigzag	Zigzag	Zigzag
Years of sampling	NA	5	10	10	10	10	5	10	10	5	5
Duration of sampling	NA	Jan-Aug	Jan-Aug	Year-round	Jan-Aug	SO winter	SO winter	Year-round	SO winter	Year-round	SO winter
Additional observations	NA	2,075	4,150	4,150	44,250	25,395	5,022	7,600	2,500	11,400	3,800
Global coverage increase (%)	NA	0.01	0.02	0.02	0.3	0.1	0.03	0.04	0.01	0.07	0.02
Mean bias (µatm)											
Testbed period (1982-2016)											
Globally	0.63	0.59	0.59	0.52	0.53	0.39	0.57	0.51	0.51	0.45	0.44
NORTH (35°N-90°N)	0.11	0.24	0.20	0.25	0.20	0.17	0.16	0.16	0.16	0.12	0.20
MID (35°S-35°N)	0.23	0.21	0.22	0.14	0.20	0.15	0.23	0.20	0.18	0.13	0.18
SOUTH (90°S-35°S)	1.4	1.3	1.2	1.1	1.1	0.80	1.2	1.1	1.1	1.0	0.87
SO winter months (JJA)	1.3	1.2	1.2	1.1	1.1	0.90	1.2	0.93	1.0	0.94	0.95
SO summer months (DJF)	0.070	0.11	0.15	0.10	0.15	0.019	0.11	0.25	0.073	0.16	0.066
2006-2012-2016											
Globally	0.51*	0.27	0.34	0.28	0.19	0.03	0.21	0.23	0.24	0.17	0.07
SOUTH (90°S-35°S)	1.6*	0.93	1.1	1.0	0.72	0.37	0.73	0.89	0.92	0.67	0.55
SOUTH (90°S-35°S) Jan, Jul, Aug	4.2*	2.6	2.7	2.8	2.2	1.8	2.5	1.8	2.4	1.2	2.0
Mean RMSE (µatm)											
Testbed period (1982-2016)											
Globally	11.8	11.7	11.8	11.7	11.7	11.6	11.7	11.5	11.6	11.5	11.6
NORTH (35°N-90°N)	13.0	13.0	13.0	13.0	13.0	13.0	13.1	13.0	13.0	13.0	13.0
MID (35°S-35°N)	11.7	11.7	11.7	11.7	11.7	11.7	11.7	11.7	11.7	11.7	11.7
SOUTH (90°S-35°S)	11.5	11.3	11.4	11.2	11.1	11.0	11.3	10.7	11.0	10.6	11.0
2006-2012-2016											
Globally	11.6*	11.6	11.4	11.3	11.3	11.2	11.6	11.0	11.2	11.1	11.4
SOUTH (90°S-35°S)	11.4*	11.1	11.0	10.7	10.4	10.9	10.4	10.0	10.4	9.7	10.6
SOUTH (90°S-35°S) Jan, Jul, Aug	12.0*	11.3	11.2	10.9	10.5	10.3	11.1	10.3	10.6	9.6	10.3

Table 1. Overview of the different sampling experiments tested in this study, and mean bias and RMSE (in µatm) for various time periods, latitude bands for all runs. Bold values represent the best score for each category. ‘One-lat’ = ‘one-latitude’ track; incorporates the Saildrone USV route from Sutton et al. (2021). ‘Zigzag’ = potential meridional sampling. ‘Additional observations’ = number of 1°x1° monthly Saildrone USV observations in addition to SOCAT. J-A= January-August. YR = year-round. W = southern hemisphere winter. x4, x5, x10 and x13 = four, five, ten and 13 USVs. SO winter = Southern Ocean winter months, i.e., June, July, August and also including September. *Average value of the mean of 2006-2016 and 2012-2016. The global coverage increase was calculated based on the total number of available 1982-2016 monthly 1°x1° observations from SOCAT (262,204 observations) and the Large Ensemble Testbed (17,290,470 observations).

2.5 Air-sea CO₂ flux

To assess the global ocean carbon sink associated with our pCO₂ reconstructions, air-sea CO₂ exchange was calculated for 1985 onward. Here, we computed air-sea CO₂ fluxes using the bulk formulation with python package Seaflux.1.3.1 (<https://github.com/lukegre/SeaFlux>; Gregor et al. 2021; Fay et al., 2021). We calculated global and Southern Ocean flux in the same manner for 1) the testbed ‘model truth’, 2) the ‘SOCAT-baseline’ and 3) the 10 experimental USV runs.

The net sea-air CO₂ flux was estimated using:

$$\text{Flux} = k_w \cdot \text{sol} \cdot (\text{pCO}_2^{\text{ocn}} - \text{pCO}_2^{\text{atm}}) \cdot (1 - \text{ice})$$

where ‘k_w’ is the gas transfer velocity, ‘sol’ is the solubility of CO₂ in seawater (in units of mol m⁻³ µatm⁻¹), ‘pCO₂^{ocn}’ is the partial pressure of surface ocean carbon (in µatm), either from the ‘model truth’ or from the reconstructions, and pCO₂^{atm} (in µatm) is the partial pressure of atmospheric CO₂ in the marine boundary layer. For GFDL, we used direct model output of pCO₂^{atm}, while for CESM and CanESM2, pCO₂^{atm} was calculated individually, as the product of

Run name	5Y J-A	10Y J-A	10Y YR	x13
Saildrone track	One-lat	One-lat	One-lat	
Years of sampling	5	10	10	
# of Saildrones	1	1	1	
Duration of sampling	Jan-Aug	Jan-Aug	Year-round	
Total observations	2,075	4,150	4,150	
Global coverage increase (%)	0.01	0.02	0.02	

- Deleted: Saildrone USV sampling patterns
- Formatted: Font: 10 pt
- Deleted: using the XGBoost Machine Learning algorithm (Gloege et al., 2021; Bennington et al., 2022a) to estimate surface ocean pCO₂
- Deleted: The ‘one-latitude’ (
- Deleted: o
- Formatted: Font: 10 pt
- Deleted:) track
- Deleted: ,
- Deleted: while the
- Deleted: z
- Deleted: track represents
- Deleted: future
- Deleted: (see Fig. 2)
- Deleted: The total
- Deleted: number of USV
- Deleted: (in bold)
- Deleted: represent
- Formatted: Pattern: Clear
- Formatted: Pattern: Clear
- Formatted: Pattern: Clear
- Formatted: Pattern: Clear
- Formatted: Pattern: Clear
- Formatted: Pattern: Clear
- Formatted: Pattern: Clear
- Deleted: Note that all runs also included SOCAT coverage.
- Deleted:

374 surface $x\text{CO}_2$ and sea level pressure (the contribution of water vapor pressure was corrected for in
375 [CESM and GFDL](#)). Finally, to account for the seasonal ice cover in high latitudes, the fluxes were
376 weighted by 1 minus the ice fraction ('ice'), i.e., the open ocean fraction. Inputs to the calculation
377 include EN4.2.2 salinity (Good et al., 2013), SST and ice fraction from NOAA Optimum
378 Interpolation Sea Surface Temperature V2 (OISSTv2) (Reynolds et al., 2002), and surface winds
379 and associated wind scaling factor from the European Centre for Medium-Range Weather
380 Forecasts (ECMWF ERA5 sea level pressure (Hersbach et al., 2020). Results presented show the
381 global and Southern Ocean (< 35° S) fluxes in units of Pg C yr⁻¹.

Deleted: pCO₂^{atm} from CESM was corrected for

382 Note that, reconstructions of pCO₂ for the 'SOCAT~~-~~baseline' and the experimental USV
383 runs are limited in their spatial extent to the open ocean (see [Sect. 2.1](#); excluding coastal areas, the
384 Arctic Ocean and marginal seas). The same mask was thus also applied when calculating the flux
385 of the 'model truth', prior to comparison with the reconstructions.

Deleted:

386 3. Results

387 3.1 Performance metrics for the 'SOCAT~~-~~baseline' reconstruction

Deleted:

388 The mean bias for the entire testbed period (i.e., 1982-2016) is 0.63 μatm globally ([Fig. 3a](#)) and
389 1.4 μatm for the Southern Ocean (< 35° S; [Table 1](#)). Bias is much closer to zero for the mid-
390 [latitudes](#) (between 35° S and 35° N; 0.23 μatm) and northern latitudes (> 35° N; 0.11 μatm) ([Fig.](#)
391 [3a](#)). There is a significant difference in bias considering southern hemisphere winter months (June,
392 July, August) versus summer months (December, January, February), with a global mean bias (for
393 1982-2016) of 1.3 μatm compared to 0.07 μatm , respectively ([Table 1](#)), due to the sparseness of
394 SOCAT observations from the southern hemisphere during the harsh winter season ([Fig. S5a](#)).
395 The mean RMSE for the entire testbed period (i.e., 1982-2016) is 11.8 μatm globally ([Fig. 3b](#)) and
396 11.5 μatm for the Southern Ocean ([Table 1](#)). RMSE is highest in the Eastern Tropical and
397 Southeastern Pacific Ocean and in the Southern Ocean, where the algorithm generally
398 overestimates pCO₂ (i.e., positive bias; [Fig. 3a](#)), with some exceptions in the Atlantic section. This
399 is consistent with the areas significantly undersampled by SOCAT ([Fig. S5b](#)). Except for these
400 areas, RMSE and bias is generally low (close to zero) in the open ocean, but show higher values
401 along coastlines ([Fig. 3b](#)).

Deleted: S

Deleted: S

Deleted: 3

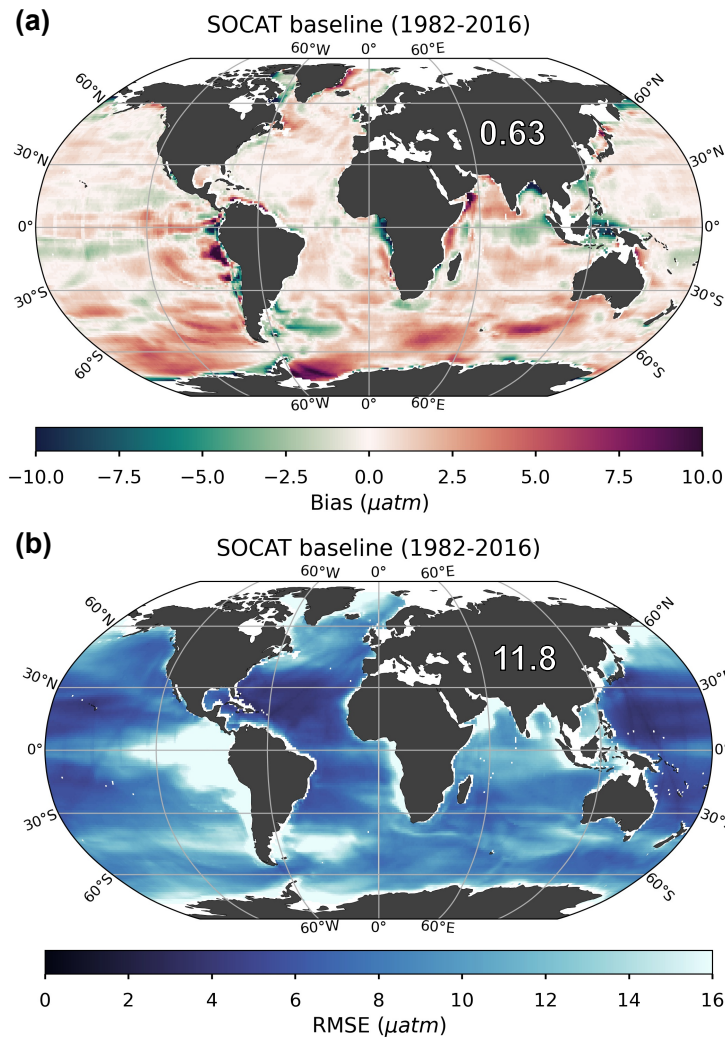
Deleted: 7

Deleted: 9

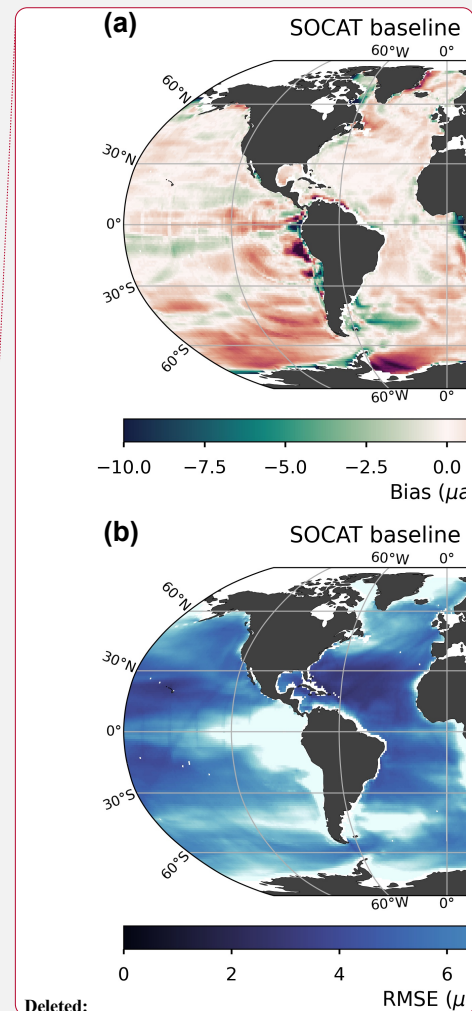
Deleted: 8

Deleted: S

Deleted: 3



413
414 **Figure 3: Bias (a) and root-mean-squared error (RMSE) (b) for the 'SOCAT-baseline' (i.e., no USV) over the period**
415 **of 1982 through 2016.** The global mean bias and RMSE is 0.63 μatm and 11.8 μatm , respectively. Note that only the
416 open ocean was considered in the reconstruction, so several areas were masked out prior to algorithm processing, such
417 as the Arctic Ocean, coastal areas and marginal seas (no data; white areas in figures).



Deleted:

Deleted: B

Deleted: when comparing the baseline machine learning reconstruction with the testbed 'model truth', averaged over the 75 ensemble members for the period of 1982 through 2016. The testbed was sampled based on SOCAT observations only (i.e., no USV).

Deleted: 7

Deleted: 9

Deleted: Red and green areas in **a** indicate regions where the reconstruction is biased high (i.e., overestimates pCO_2) and low (i.e., underestimates pCO_2), respectively. Generally, RMSE is highest in the East and South Pacific Ocean and in the Southern Ocean, where the algorithm also generally overestimates pCO_2 (positive bias; **a**).

435 3.2 Reconstruction improvements with Saildrone USV additions

436 Our presentation of global maps is limited to runs ‘x5_5Y_W’ (5,022 monthly 1°x1° observations)
437 and ‘Z_x4_10Y_YR’ (7,600 monthly 1°x1° observations). These runs were selected as they
438 represent observational schemes that are realistic in the near-term future considering logistics and
439 cost level, both non-meridional and meridional sampling, and different approaches to observing
440 duration and seasonal coverage. For the remaining runs, equivalent maps can be found in the
441 **Supplement**.

442 3.2.1 Bias

443 All Saildrone USV runs show a reduction in bias compared to the global mean 1982-2016
444 ‘SOCAT-baseline’ (Figs. 4a, S6). The improvement in bias is mainly due to lower reconstructed
445 pCO₂ values at southern latitudes, where the ‘SOCAT-baseline’ reconstruction generally
446 overestimates pCO₂ (Fig. 3a). The global mean bias for ‘zigzag’ run ‘Z_x4_10Y_YR’ is 0.51
447 μatm, a higher improvement (19 %) over the ‘SOCAT-baseline’ compared to the ‘one-latitude’
448 run ‘x5_5Y_W’ (11 % mean improvement; mean bias = 0.57 μatm;) (Fig. 4a; Table 1). Generally,
449 the ‘zigzag’ runs show higher improvements from the ‘SOCAT-baseline’ (19-31 % improvement;
450 resulting mean bias = 0.44-0.51 μatm) compared to the ‘one-latitude’ runs (7-19 % improvement;
451 resulting mean bias = 0.52-0.59 μatm) (Fig. S6; Table 1). However, the ‘one-latitude’-run
452 ‘x13_10Y_W’ that samples southern hemisphere winter months only, stands out with the lowest
453 global mean bias of 0.39 μatm, representing a 39 % mean improvement from the ‘SOCAT-
454 baseline’, as well as reduced spread across the 75 ensemble members (Table 1; Fig. S6; S8). This
455 run, however, has three or five times more observations (25,395) than ‘Z_x4_10Y_YR’ and
456 ‘x5_5Y_W’, respectively.

457 Compared to the entire testbed period, even larger improvements in global mean bias are
458 shown for the period of Saildrone USV additions (2006-2016 and 2012-2016; Figs. 4a vs. 4b,
459 Figs. S6 vs. S7). Compared to the ‘SOCAT-baseline’, run ‘x13_10Y_W’ results in a mean bias
460 improvement of 95 %, while the remaining ‘one-latitude’ runs and the ‘zigzag’ runs show mean
461 improvements up to 63 % and 85 %, respectively (Fig. S7).

462 Perhaps surprisingly, there is not a strong connection between the global or Southern Ocean
463 mean bias and the number of added USV observations (Fig. 5). The ‘one-latitude’ ‘high-sampling’

Deleted:

Deleted: 4

Deleted:

Deleted: S

Deleted:

Deleted: 4

Deleted: S

Deleted:

Deleted: S

Deleted: 4

Formatted: Font: Not Bold

Formatted: Not Highlight

Deleted: 4

Deleted: 5

Deleted:

Deleted: 5

478 run 'x13_10Y_J-A' (44,250 observations) show similar mean bias or is outperformed by all
479 'zigzag' runs as well as the 'one-latitude'-runs that restrict sampling to southern hemisphere winter
480 months (i.e., 'x5_5Y_W' and 'x13_10Y_W').

481 Considering the change in bias from year-to-year, the 'SOCAT-baseline' shows positive
482 bias at all latitudes in the beginning of the testbed period, before improvement occurs around 1990
483 (Fig. 6a). This is consistent with increasing SOCAT sampling with time for the period considered
484 here (i.e., up to 2016; Fig. S5c). As SOCAT observations are biased towards the northern
485 hemisphere (Fig. S5a, b), bias in the Southern Ocean (< 35° S) increases significantly starting in
486 the 2000s and remains high until the end of the testbed period (Fig. 6a). By adding USV sampling,
487 bias in the Southern Ocean improves over the 'SOCAT-baseline' around year 2000 (Fig. 6b-d;
488 Fig. S9), up to 6-12 years before to the introduction of additional samples in either 2006 or 2012.
489 This improvement is shown for the majority of the 75 ensemble members (Fig. S10). Run
490 'Z_x10_5Y_W', which has the lowest mean bias out of the 'zigzag' runs (Fig. 5), shows
491 improvement even further back in time, until the beginning of the testbed period (Fig. S9). While
492 the annual mean bias of the 'zigzag' runs varies rather consistently, there is a larger spread across
493 the 'one-latitude' runs (Fig. 6d).

Deleted:

Deleted: year

Deleted: time

Deleted: 3

Deleted: 3

Deleted:

Deleted: 6

Deleted: prior

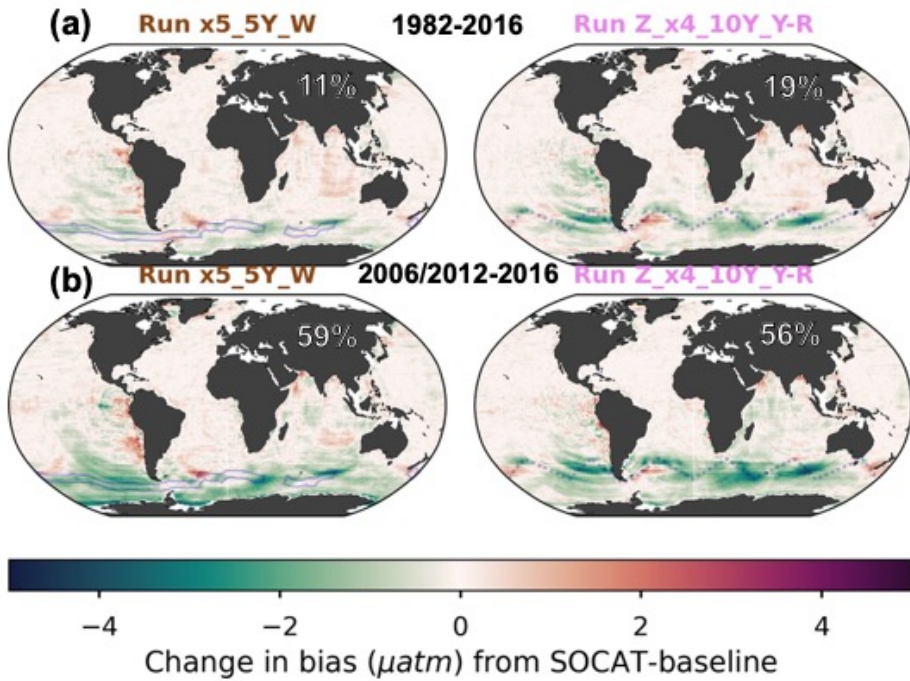
Formatted: Font: Bold

Deleted: 6

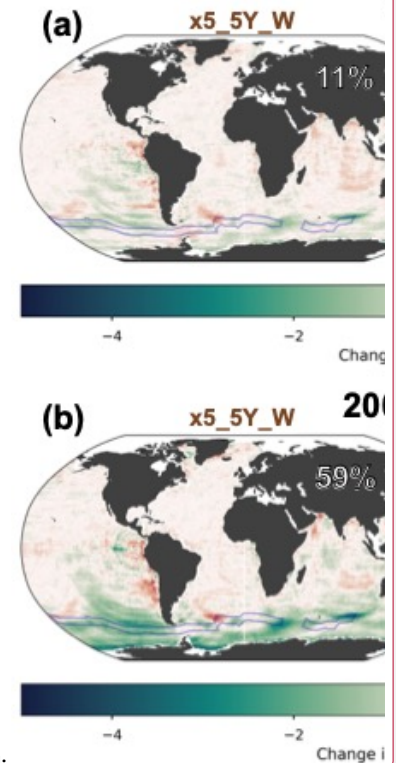
Deleted: vary

Deleted: in a similar manner

Deleted: between



506
507
508 **Figure 4:** Change in bias when comparing run 'x5 5Y W' and 'Z x4 10Y YR' to the 'SOCAT baseline'
509 reconstruction, averaged over the duration of the testbed period (a; 1982-2016) and the period of USV additions (b;
510 2006-2012 or 2012-2016). The percent global improvement in absolute bias is shown on each panel.

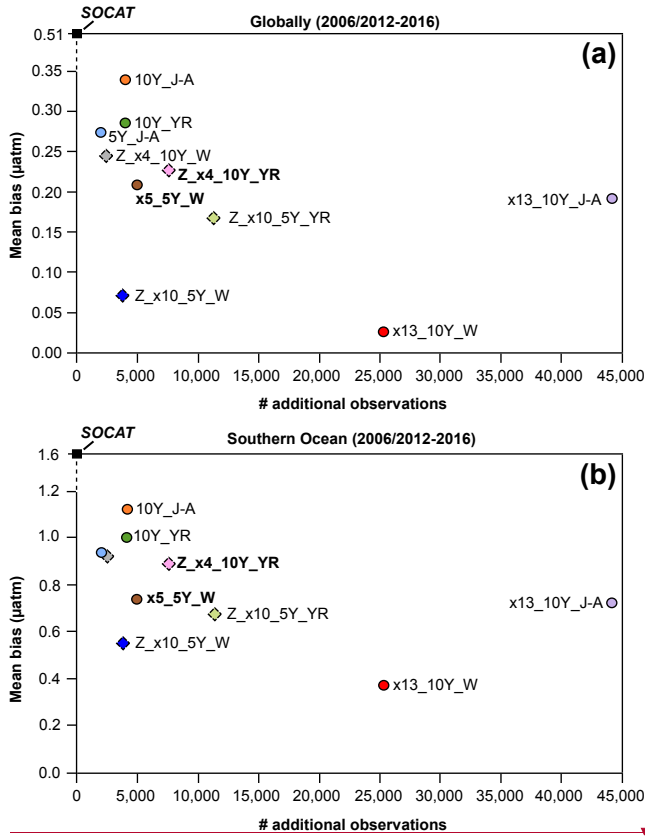


Deleted:

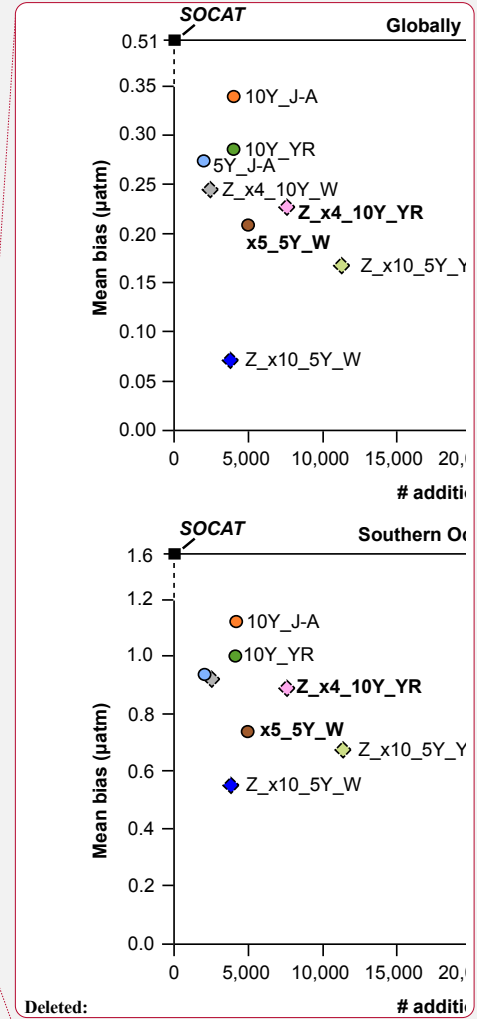
Deleted:

Deleted: Negative change in bias is found across the southern latitudes, indicating an improvement compared to the SOCAT baseline that overestimates pCO₂ (Figure 3a).

Deleted: Note that improvement is greater in the period of Saildrone USV additions compared to the entire testbed period. ...

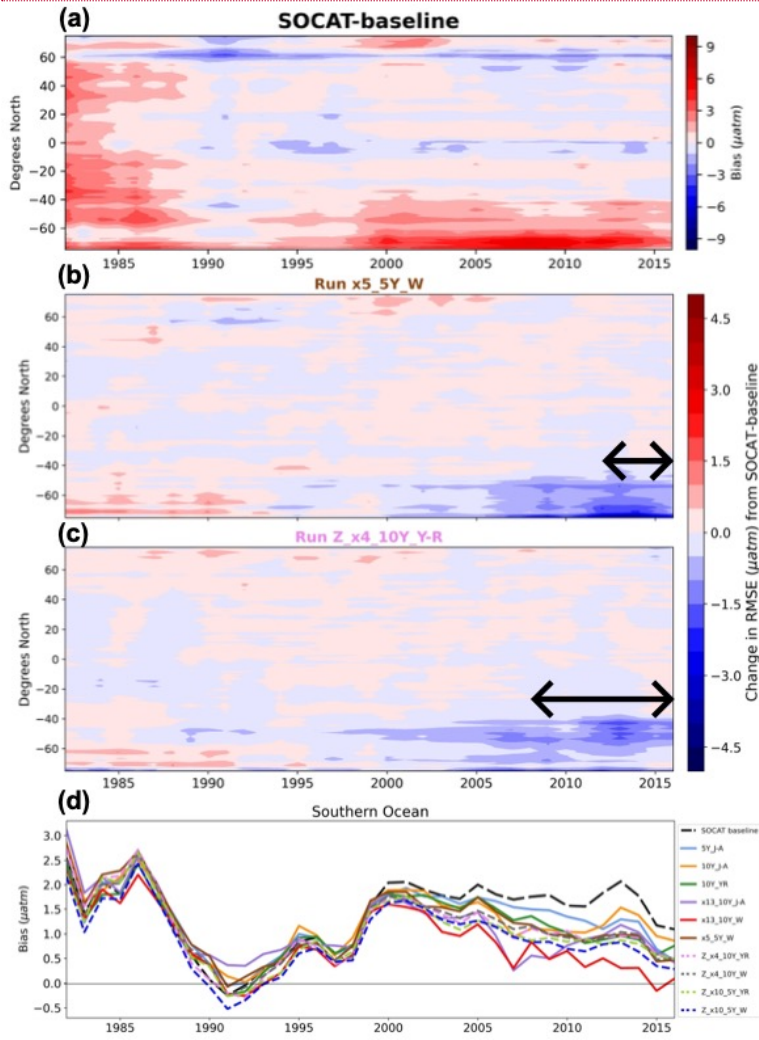


519
 520 **Figure 5:** Mean bias globally (a) and for the Southern Ocean (b) for the duration of Saildrone USV sampling (2006-
 521 2016 or 2012-2016) for all runs presented in **Table 1**. Circles represent runs using the 'one-latitude' track, while
 522 diamonds represent 'zigzag' runs. Runs highlighted in bold correspond to the two selected runs mapped in **Figure 4**,
 523 **6**, **7** and **9**. Global (0.51 µatm) and Southern Ocean (1.6 µatm) bias values shown for the 'SOCAT baseline' (black
 524 squares) represent a mean of values for 2006-2016 (global = 0.52 µatm, S. Ocean = 1.63 µatm) and 2012-2016 (global
 525 = 0.51 µatm, S. Ocean = 1.56 µatm). '# additional observations' = number of monthly 1°x1° USV observations in
 526 addition to SOCAT. Box plots illustrating the spread across the 75 ensemble members are shown in **Fig. S8**.



Deleted: # additi
 Deleted: (Sutton et al., 2021)
 Deleted:
 Deleted: The SOCAT baseline run included 261,733 monthly 1°x1° observations.
 Formatted: Font: Bold

532

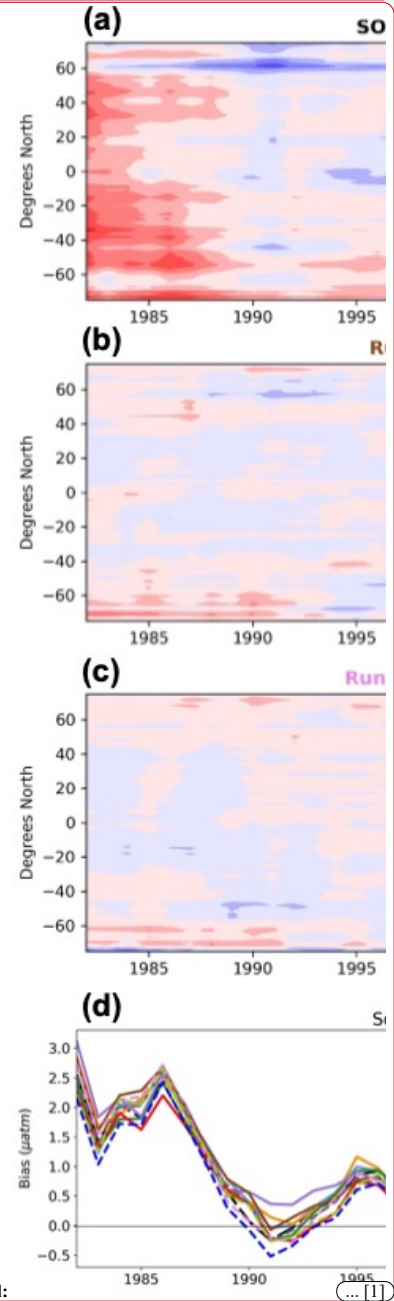


533

534 **Figure 6:** Zonal mean, annual mean Hovmöller of bias for the 'SOCAT-baseline' (a). Change in bias for run
 535 'x5_5Y_W' (b) and 'Z_x4_10Y_YR' (c) compared to the 'SOCAT-baseline' shown in (a). Improvement in bias in
 536 the Southern Ocean expands back in time well beyond the duration of USV additions for both runs (shown by arrows
 537 on each panel). Annual mean bias for the Southern Ocean (> 35° S) for all runs (d).

538

Deleted: Overall, there is not a strong correlation between bias and the number of observations, or duration of sampling.



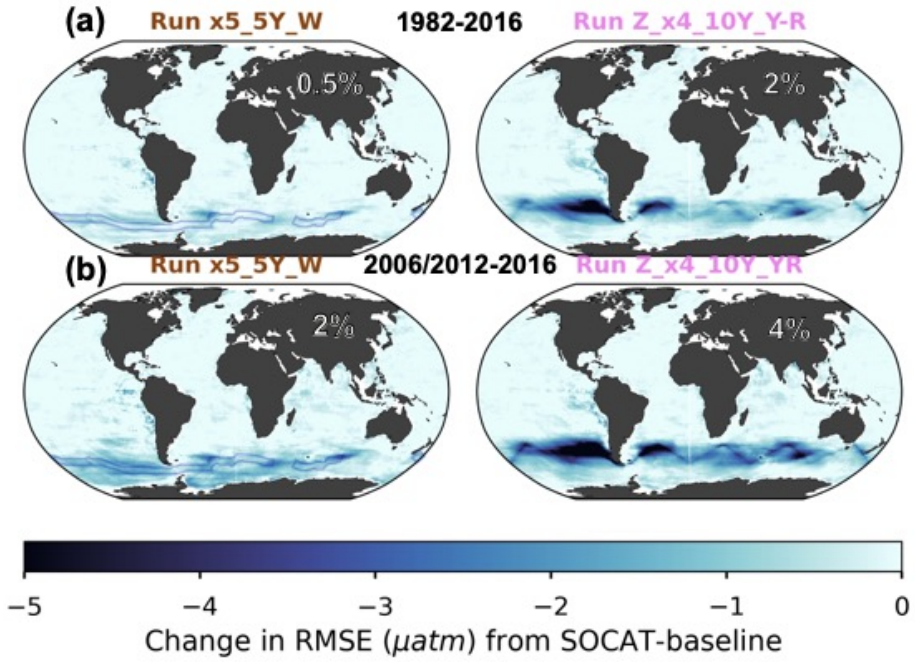
Deleted:

578 3.2.2 Root-mean squared error (RMSE)

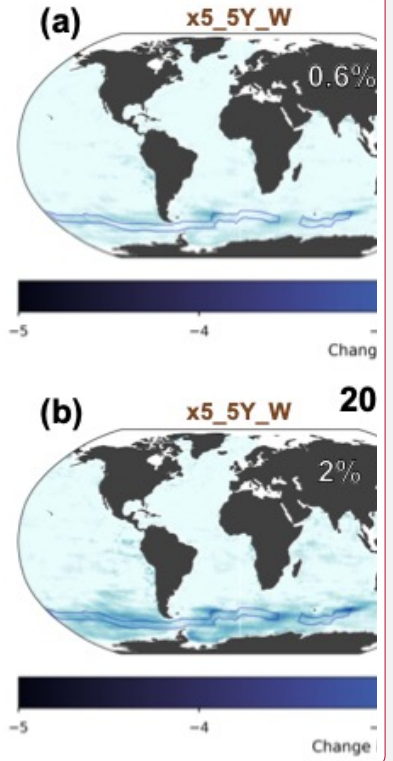
579 Similar to bias, improvements in RMSE are most significant during the period of USV additions
580 and within the Southern Ocean (Fig. 7a vs. 7b). For the duration of USV additions, the ‘one-
581 latitude’ runs show improvements in global mean RMSE of 1-3% (0.1-1% for 1982-2016), while
582 the ‘zigzag’ runs show higher improvements between 2-5% (1-3% for 1982-2016) (Figs. 7, S11,
583 S12). Mean RMSE is further reduced in the Southern Ocean by up to 16%, and during southern
584 hemisphere winter months (JJA) up to 21% (run ‘Z x10 5Y YR’; mean RMSE of 9.6 μatm ;
585 Table 1). There is minimal change in RMSE (or bias) during southern hemisphere summer months
586 (DJF; Fig. S13). The two ‘zigzag’ runs sampling year-round (‘Z x4 10Y YR’ and
587 ‘Z x10 5Y YR’) have the lowest RMSE values both globally and in the Southern Ocean (Fig. 8).
588 The spread across the 75 testbed members for each experiment is shown in Figure S14.

589 The ‘zigzag’ runs, as well as the ‘high-sampling’ ‘one-latitude’-runs (i.e., ‘x13_10Y_J-A’
590 and ‘x13_10Y_W’), show improvements compared to the ‘SOCAT-baseline’ from the initiation
591 of sampling (Figs. 9, S15, S16). The year-round ‘zigzag’ runs, however, show improvement in the
592 Southern Ocean from the beginning of the testbed period (Figs. 9c, d, S15). RMSE improvements
593 back in time are greater for all runs in the southern hemisphere winter months (Fig. S17).

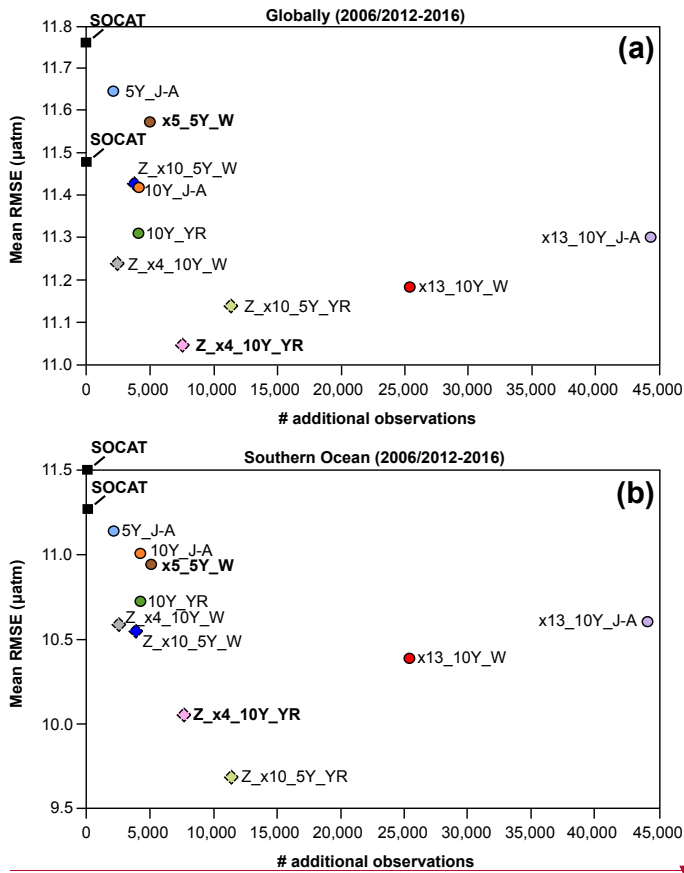
- Deleted: 4
- Deleted: 3
- Deleted: 2
- Deleted: 3
- Deleted: 8
- Deleted: 2
- Deleted: 7
- Deleted: 8
- Deleted: in the Southern Ocean by
- Deleted: 6
- Deleted: 6
- Deleted: 9
- Deleted: 5
- Deleted: 9
- Deleted: ’
- Formatted: Font: Bold
- Deleted:
- Deleted: 0
- Formatted: Font: Not Bold
- Deleted: 0
- Deleted: more significant
- Deleted: 1



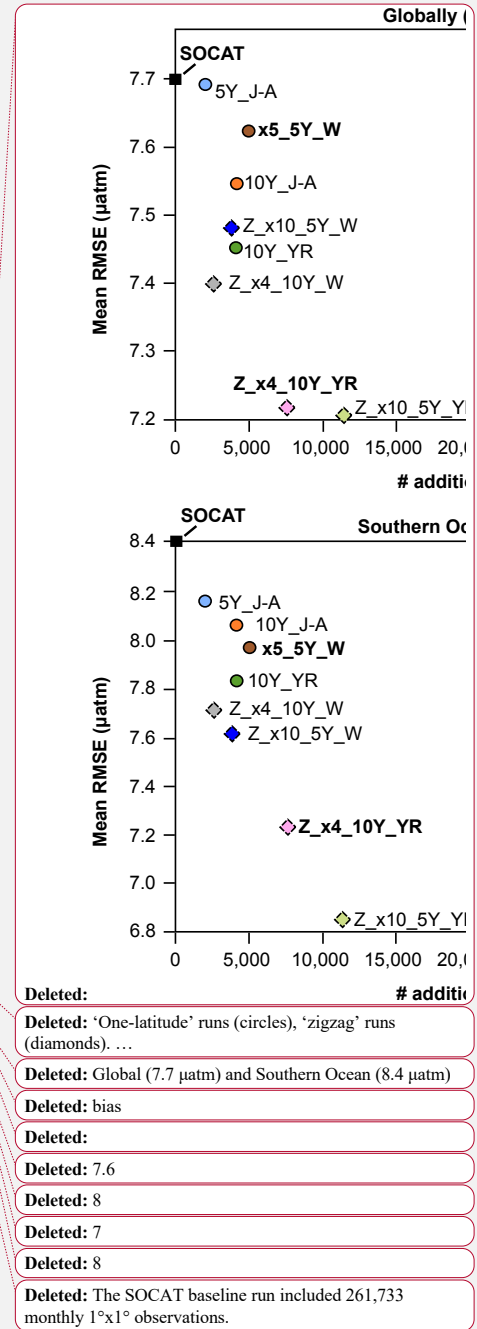
614
 615 **Figure 7:** Change in RMSE when comparing run 'x5 5Y W' and 'Z x4 10Y YR' to the 'SOCAT-baseline',
 616 averaged over the duration of the testbed period (a; 1982-2016) and the period of Saildrone USV additions (b; 2006-
 617 2012 or 2012-2016). The percent global improvement is shown on each panel.



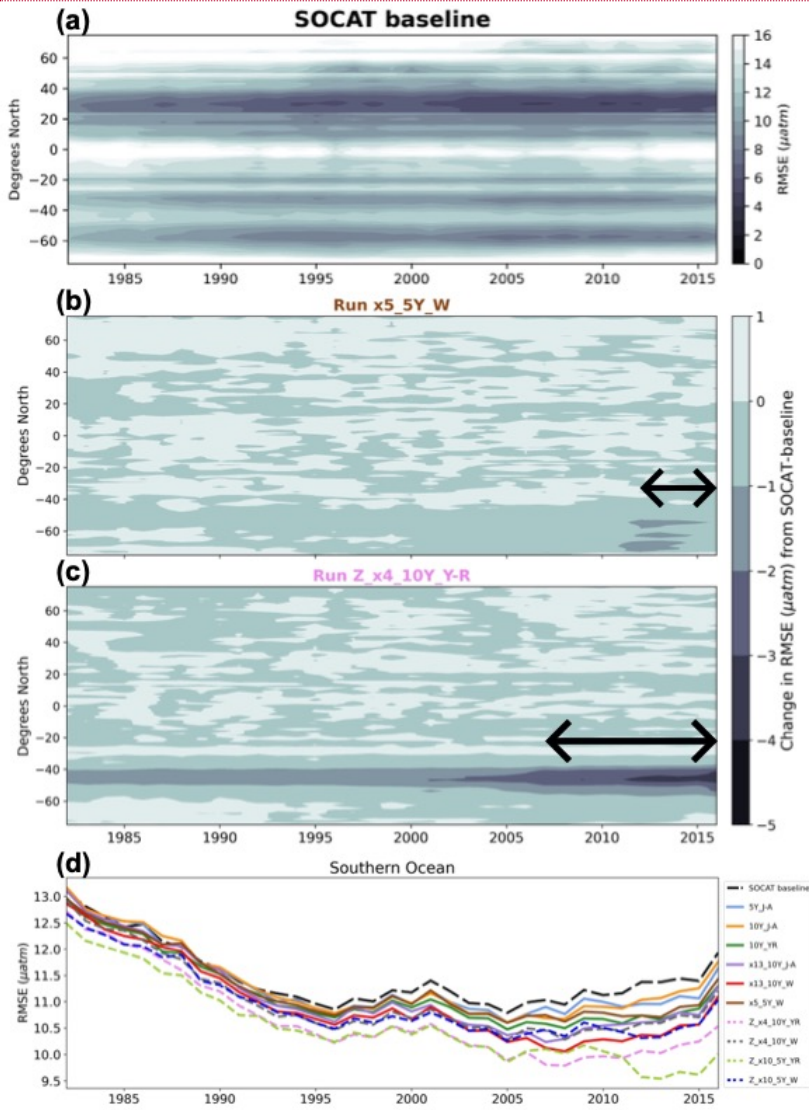
Deleted:
 Deleted:
 Deleted: reconstruction
 Deleted: Improvement in RMSE occurs mainly in southern latitudes (<35°S), where the baseline reconstruction shows high RMSEs (Fig. 3b).
 Deleted: Note the greater improvement for the period of USV additions compared to the entire testbed period.



626
 627 **Fig. 8:** Mean RMSE globally (a) and for the Southern Ocean (< 35° S; b) for the duration of Saildrone USV sampling
 628 (2006-2016 or 2012-2016) for all runs presented in Table 1. Circles represent runs using the 'one-latitude' track, while
 629 diamonds represent 'zigzag' runs. Runs highlighted in bold correspond to the two selected runs mapped in Figure 4,
 630 6, 7 and 9. RMSE values shown for the 'SOCAT baseline' (black squares) represent a mean of values for 2006-2016
 631 (global = 11.5 μatm , S. Ocean = 11.3 μatm) and 2012-2016 (global = 11.8 μatm , S. Ocean = 11.5 μatm). '# additional
 632 observations' = number of monthly 1°x1° USV observations in addition to SOCAT. Box plots illustrating the spread
 633 across the 75 ensemble members are shown in Fig. S14.



646

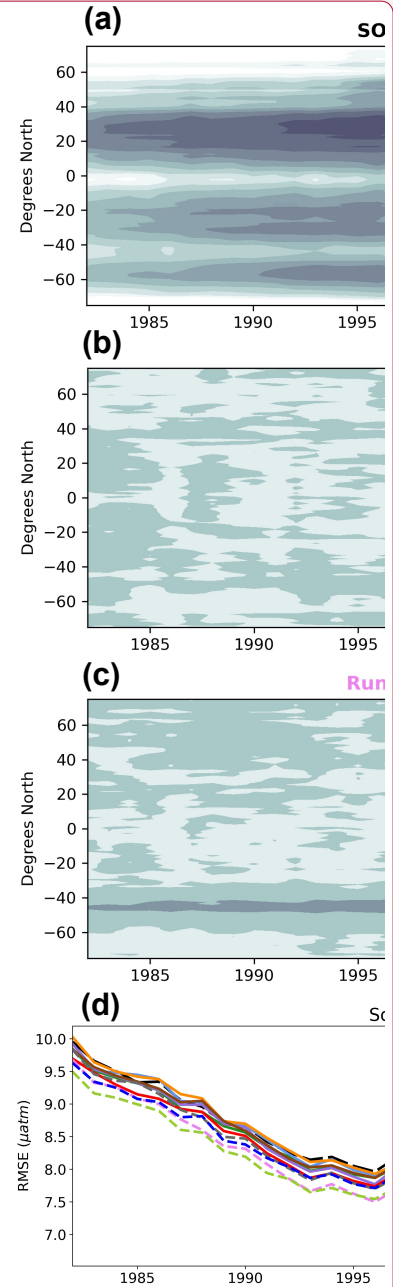


647

648 **Figure 9:** Zonal mean, annual mean Hovmöller of RMSE for the 'SOCAT-baseline' (a). Change in RMSE for run
 649 'x5_5Y_W' (b) and 'Z_x4_10Y_YR'(c) compared to the 'SOCAT-baseline'. Run 'Z_x4_10Y_YR' shows
 650 improvement in RMSE within the Southern Ocean, which expand well beyond the duration of Sairdronc USV
 651 additions (shown by arrow on panel). Annual mean RMSE for the Southern Ocean (> 35° S) for all runs (d).

Deleted: Overall, there is not a strong correlation between increasing number of observations or duration of sampling and decreasing RMSE.

Formatted: Font: Not Italic



Deleted:

Deleted: in... 'SOCAT-...aseline' (with the testbed 'model truth', average of 75 ensemble members (...)). Dark and light areas represent regions where RMSE is low and high, respectively. RMSE is highest at latitudes > 60° S, > 60° N and around 40° S and the equator. RMSE is higher at all latitudes in the beginning of the testbed period, before some improvement occurs in the 1990s. ...change in RMSE forof...run 'x5_5Y_W' (b) and 'Z_x4_10Y_YR'(c) compared to the 'SOCAT-...aseline' reconstruction shown in (a)... Dark areas represent regions where the change in RMSE is negative, i.e., where the Sairdronc USV sampl... [2]

Formatted: Line spacing: single

706 3.3 Impact on the air-sea CO₂ flux with Saildrone USV additions

707 Air-sea flux was calculated in the same manner for both the ML reconstructions and the ‘model
708 truth’, which allows for the isolation of the impact of different sampling strategies, as mediated by
709 the pCO₂ reconstruction, on fluxes (see Sect. 2.5). These flux estimates are made to inform
710 understanding of the errors that may exist in CO₂ flux estimates derived from pCO₂
711 reconstructions, and how new sampling could address these errors. Flux estimates represent the
712 average of the 75 members of the LET in each case, and are not estimates of real-world fluxes.

713 Compared to the ‘model truth’, the ‘SOCAT-baseline’ reconstruction underestimates the
714 global and Southern Ocean sink by 0.11-0.13 Pg C yr⁻¹ over 1982-2016 (Fig. 10; Table S1).
715 Regardless of sampling pattern, adding Saildrone USV observations increases both the global and
716 Southern Ocean mean sink compared to the ‘SOCAT-baseline’ (Figs. 10, S18). The ‘one-latitude’
717 runs show an increase of 0.01-0.03 Pg C yr⁻¹ (2-6 % strengthening) of the Southern Ocean sink
718 (1982-2016), while the ‘zigzag’ runs lead to an even stronger sink by 0.04-0.06 Pg C yr⁻¹ (7-11 %
719 strengthening) (Table S2). When averaging over the years of Saildrone USV sampling addition
720 (i.e., 2006-2012 and 2012-2016), the Southern Ocean sink increases up to 0.09 Pg C yr⁻¹ (14 %
721 strengthening) for the ‘one-latitude’ runs and up to 0.1 Pg C yr⁻¹ (15 % strengthening) for the
722 ‘zigzag’ runs (Table S2). These same features are found for the global ocean (Fig. S18; Table
723 S2).

724 All of the ‘zigzag’ runs quite closely match both the global and Southern Ocean ‘model
725 truth’ air-sea CO₂ flux for the duration of sample additions (Figs. 10, S18). Except for the first
726 couple of years of sample addition for the ‘high-sampling’-run ‘x13_10Y_J-A’, none of the ‘one-
727 latitude’ runs can match the ‘model truth’ air-sea CO₂ flux, instead they all underestimate the flux
728 (Figs. 10, S18). The ‘zigzag’ runs have impact on the air-sea flux from an earlier date, starting to
729 pull the results away from the ‘SOCAT-baseline’ and toward the ‘model truth’ already in the late-
730 1990s, while the ‘one-latitude’ runs do the same about a decade later (Figs. 10, S18).

Deleted: direct comparison of the differences in

Formatted: Subscript

Deleted: These fluxes

Deleted:

Deleted: 2

Deleted:

Deleted: 2

Deleted: 3

Deleted: 3

Deleted: 2

Deleted: 3

Deleted: 2

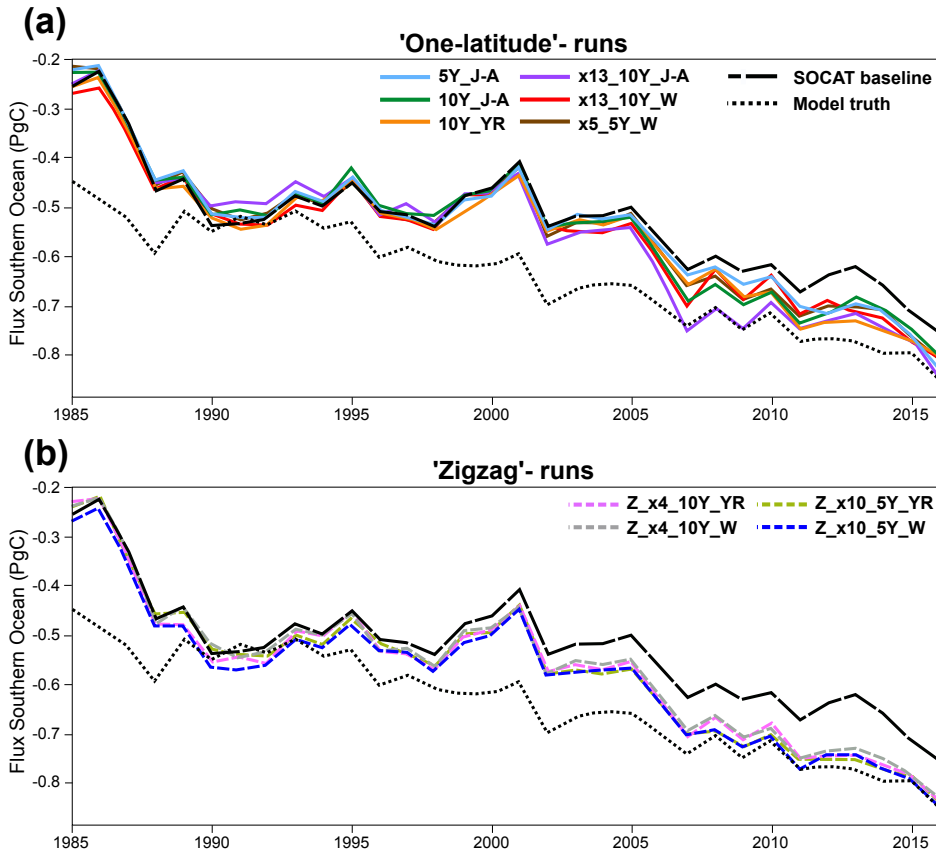
Deleted: are able to

Deleted: as

Deleted: 2

Deleted:

Deleted: 2



747
748 **Figure 10:** Southern Ocean (< 35° S) annually averaged air-sea CO₂ flux for the 'SOCAT baseline' (black dashed
749 line), 'model truth' (black dotted line) 'one-latitude' runs (a; solid lines) and 'zigzag' runs (b; dashed lines).

750
751
752 **4. Discussion**

753 We have tested the pCO₂-Residual reconstruction method with the Large Ensemble Testbed (LET)
754 to estimate its fidelity and understand how new samples could increase skill. We find that,
755 regardless of the chosen Sailability USV sampling pattern, the reduction in **mean bias** and **mean**
756 **RMSE** compared to the 'SOCAT baseline' is most prominent within the Southern Ocean (< 35°
757 S) during the period of which Sailability USV observations were added (Figs. 4, 6, 7, 9). However,
758 it is important to mention that additional Southern Ocean sampling also improves pCO₂

Deleted:

Deleted: , averaged over the 75 ensemble members

Deleted: Compared to the SOCAT baseline, regardless of sampling pattern, the Sailability USV additions lead to an increased ocean sink. The 'zigzag' runs generate a stronger sink compared to the 'one-latitude' runs, and closely match the 'model truth' for the duration of sample additions.

Deleted: both

Deleted:

768 reconstructions globally (Figs. 5a, 8a). Based on our experiments, a combination of factors
769 improve global and Southern Ocean pCO₂ reconstructions, including the type of sampling pattern
770 and seasonality of sampling, and to some extent, the number of additional observations.
771 Importantly, increasing the number of observations or duration of sampling (5 vs. 10 years) is not
772 the sole determining factor for improving the reconstructions (Figs. 5, 8). This is best demonstrated
773 by the ‘high-sampling’-run ‘x13_10Y_J-A’ (44,250 observations), which does not provide
774 significantly better reconstructions, or is even outperformed, by runs with 2-18 times fewer
775 observations. The runs that produce lower mean RMSE do include data throughout southern
776 hemisphere winter (Figs. 8, 9d). Run ‘x13_10Y_J-A’ does not include more than a few
777 observations in the month of August, as it follows the temporal pattern of the real-world ‘one-
778 latitude’ Saildrone USV expedition (Fig. S2; Sutton et al., 2021). The ‘one-latitude’ runs ‘10Y_J-
779 A’ and ‘10Y_YR’ are directly comparable in terms of sample duration, spatial extent and number
780 of observations (Table 1), but the latter, which covers all months, always shows lower mean
781 RMSE and bias (Figs. 5, 6d, 8, 9d). These examples attest to the importance of addressing the
782 issue of significant undersampling in the Southern Ocean during the winter season (Figs. S5a, b).

783 Another important comparison is the ‘one-latitude’-run ‘x5_5Y_W’ (5,022 observations)
784 and ‘zigzag’-run ‘Z_x10_5Y_W’ (3,800 observations) that both sample during southern
785 hemisphere winter months over a five-year period (Table 1), where the ‘zigzag’-run consistently
786 performs better even though it includes fewer observations (Figs. 5, 8). Most of the runs that
787 perform similar to, or outperform, the above-mentioned ‘high-sampling’-run ‘x13_10Y_J-A’
788 (44,250 observations), sample in a ‘zigzag’ pattern. Out of all 10 runs, the ‘year-round’ ‘zigzag’
789 runs (‘Z_x4_10Y_YR’ and ‘Z_x10_5Y_YR’) are most able to reduce the mean error as shown by
790 the lowest RMSE values (Figs. 8, 9d). A recent study performed similar sampling experiments as
791 shown here, by comparing sampling from different types of autonomous platforms to a ‘SOCAT-
792 baseline’ (Djeutchouang et al., 2022). They emphasized the importance of capturing the significant
793 differences in pCO₂ that exist across meridional gradients during summer and winter months (up
794 to 15 µatm; Djeutchouang et al., 2022). The meridional coverage provided by the ‘zigzag’ runs
795 could explain why these runs generally outperform the ‘one-latitude’ runs in our study, and show
796 significant reduction in both RMSE and bias, even though the global pCO₂ data density is raised
797 by as little as 0.01-0.07%.

Deleted: seems to be important in order to

Deleted: both the

Deleted: and

Deleted: e

Deleted: mainly

Deleted: but also

Deleted: 2-18 times less

Deleted: , but that cover the full

Deleted: 5, 6d,

Deleted: 1

Deleted: 3

Deleted: magnitude of

Deleted:

Deleted: 4

812 The greatest reduction in mean bias out of all runs is shown by run 'x13_10Y_W' (Figs.
813 5, 6d), which represents 'one-latitude' 'high-sampling' (i.e., 25,395 observations) during southern
814 hemisphere winter months only. This sampling strategy seems thus to have a higher ability to
815 reduce the ML model's tendency to overestimate pCO₂ in the Southern Ocean compared to any of
816 the meridional ('zigzag') runs. However, it should be noted that run 'x13_10Y_W' covers areas
817 south of 55° S (Fig. S4), and its improvement in mean bias (and mean RMSE) is particularly
818 prevalent at these high latitudes (e.g., Figs. S7, S9, S12, S17). Whether or not this run is, in fact,
819 feasible with current or future technology is uncertain as parts of the southernmost tracks
820 potentially cover the Southern Ocean ice zone (Fig. S19), and solar radiation for solar-powered
821 platforms and sensors becomes very limited during winter south of 55° S. Furthermore, this
822 particular sampling strategy requires 13 USVs, and so would be the most costly of the observing
823 scenarios. Although run 'x13_10Y_W' demonstrates the highest reduction in mean bias out of all
824 runs, the 'zigzag' runs still reduce mean bias in the Southern Ocean by 44-65 % (vs. 77 % for run
825 'x13_10Y_W').

826 Overall, the 'zigzag' runs include significantly fewer observations, require fewer USVs,
827 collect samples over the same duration, or even half the time as run 'x13_10Y_W', cover areas
828 north of 55°S and within the ice-free zone, and show major improvement in the reconstruction of
829 pCO₂, attested to by reductions in both bias and RMSE. The 'zigzag' runs also closely match both
830 the global and Southern Ocean 'model truth' air-sea CO₂ flux for the duration of sample additions
831 (Figs. 10, S18). It also appears that the 'zigzag' runs generally have a greater impact on both the
832 pCO₂ reconstruction and the air-sea flux further back in time, starting to deviate from the 'SOCAT-
833 baseline' earlier compared to the 'one-latitude' runs (Figs. 6, 9, 10, S9, S15, S17, S18). Even the
834 'zigzag' scenarios with the least number of USVs (e.g., 'Z_x4_10Y_YR') reduces Southern Ocean
835 reconstruction bias and RMSE by up to 46 % and 11%, respectively, and could provide a basis
836 for realistic future Southern Ocean pCO₂ sampling campaigns.

837 The main motivation for improving surface ocean pCO₂ reconstructions is so that we can
838 more accurately estimate the current and future oceanic uptake of anthropogenic carbon. The
839 Southern Ocean is a significant carbon sink, but estimates of the air-sea CO₂ flux diverge
840 substantially in this region (Takahashi et al., 2009; Landschützer et al., 2014, 2015; Rödenbeck et
841 al., 2015; Williams et al., 2017; Gray et al., 2018; Gruber et al., 2019; Bushinsky et al., 2019; Long

Deleted: i

Deleted: however

Deleted: 2

Deleted: such

Deleted: 5

Deleted: 6

Deleted: 8

Deleted: 0

Deleted: 3

Deleted: thus

Deleted: less

Deleted: 2

Deleted:

Deleted: 6

Deleted: 0

Deleted: 1

Deleted: 2

Deleted: 3

860 et al., 2021; Fay and McKinley, 2021; Wu et al., 2022). Southern Ocean estimates incorporating
861 observations from biogeochemical floats have shown a significantly weaker sink compared to
862 those based only on observations from ships (Williams et al., 2017; Gray et al., 2018; Bushinsky
863 et al., 2019). Bushinsky et al. (2019) and Hauck et al. (2023) performed similar sampling
864 experiments as presented here, by comparing ML surface ocean pCO₂ reconstructions based on
865 SOCAT vs. additional SOCCOM or ideal virtual floats. These studies showed that SOCAT
866 sampling alone overestimates the CO₂ uptake in the Southern Ocean, and that additional floats
867 reduce this overestimation, leading to a decreased (weakened) ocean carbon sink. In contrast, we
868 find that the pCO₂-Residual method underestimates the CO₂ uptake with only SOCAT sampling,
869 and that adding USVs increased (strengthened) the Southern Ocean and global ocean sink by up
870 to 0.1 Pg C yr⁻¹ (Figs. 10, S18; Table S2).

871 Going forward, additional studies are needed to better understand why these results suggest
872 a different direction of the sink change with additional sampling. These differences could stem
873 from the use of different reconstruction methods assessed. Hauck et al. (2023) used the MPI-SOM-
874 FFN and CarboScope/Jena-MLS reconstruction methods, while we use the pCO₂-Residual
875 method. Another substantial difference between the studies is the models and numbers of ensemble
876 members used as the testbed. Hauck et al. (2023) use a single hindcast model, while we use 25
877 members each from three Earth System Models. We find substantial spread across these 75
878 members (Figs. S8, S10, S14, S16), indicating that model structure and internal variability
879 significantly impact results. Our study and Hauck et al. (2023) use different sampling masks and
880 approaches for the calculation of fluxes, which could also be a factor. Targeted, coordinated studies
881 using multiple reconstruction approaches with consistent testbed structures and experimental
882 approaches are clearly needed (Rödenbeck et al., 2015). Despite this need for this additional work,
883 studies do agree that additional Southern Ocean observations could significantly improve
884 reconstructions of air-sea CO₂ fluxes.

885 What else can we learn using the model testbed? The 'SOCAT-baseline' demonstrates a
886 weakening of the global and Southern Ocean carbon sink starting in the 1990s with a peak around
887 year 2000 (Figs. 10, S18), which is in broad agreement with various data products using real-world
888 SOCAT data (e.g., Gruber et al., 2019; Landschützer et al., 2015; Bushinsky et al., 2019;
889 Bennington et al., 2022; Gloege et al., 2022). Peaks in bias and RMSE coincide in time with the

Deleted: alone

Deleted: Southern Ocean

Deleted: They

Deleted: by

Deleted: ng

Deleted: the

Formatted: Subscript

Deleted: , the Southern Ocean carbon sink (mean of the period of float additions; 2015-2017) decreased (weakened) by 0.4 Pg C yr⁻¹. In contrast,

Deleted: by using a model testbed, we show that

Formatted: Subscript

Formatted: Subscript

Deleted: 2

Deleted: 3), which is a significant fraction of the uncertainty in the global ocean carbon sink (0.4 Pg C yr⁻¹; Friedlingstein et al., 2022

Deleted: Fed with real-world SOCAT data, the global mean air-sea flux estimate from the pCO₂-Residual method is similar to other available products (Bennington et al., 2022a), suggesting that other products may also underestimate the Southern Ocean carbon sink due to the spatio-temporal distribution of SOCAT data. Our experiments suggest that targeted USV observations could reduce this underestimation of the ocean carbon sink.

Formatted: Subscript

Formatted: Font: Bold, Not Highlight

Formatted: Not Highlight

Formatted: Font: Bold, Not Highlight

Formatted: Font: Bold

Formatted: Font: Bold

Formatted: Font: Bold

Formatted: Highlight

Formatted: Subscript

Deleted: ¶

Deleted:

Deleted: 2

915 weakening sink (Figs. 6d, 9d). As shown by Figure 10, this ‘low sink’ is significantly exaggerated
916 compared to the ‘model truth’. To better understand this discrepancy, we performed an additional
917 experiment based on run ‘Z_x10_5Y_YR’, but assumed sampling every year for the entire testbed
918 period (i.e., 1982-2016). There is now a significant reduction in the temporal variability of
919 reconstruction bias; with the additional 35-year USV sampling, the reconstructed Southern Ocean
920 air-sea CO₂ flux closely matches the ‘model truth’ for the entire testbed duration (Fig. S20). This
921 suggests that the large decadal variability of air-sea CO₂ fluxes since the 1980s, and the weak
922 anomaly in the Southern Ocean carbon sink in the early 2000s (Le Quéré et al., 2007; Landschützer
923 et al., 2015; Gruber et al., 2019; Bennington et al., 2022a,b; Friedlingstein et al., 2023), may be at
924 least partially attributable to undersampling of the Southern Ocean. This is in agreement with the
925 float sampling experiments performed by Hauck et al. (2023), attributing the strong decadal
926 variability to sparse and skewed SOCAT data distributions. We will further explore this issue in
927 future work. Still, this preliminary experiment suggests that interpretations of trends and variability
928 of the global and Southern Ocean carbon sink should be considered with caution.

929 5. Conclusions

930 By using the Large Ensemble Testbed (LET), we show that targeted meridional and winter
931 sampling in the Southern Ocean can improve global and Southern Ocean ML surface ocean pCO₂
932 reconstructions. Significant improvements are possible by raising the global pCO₂ data density by
933 as little as 0.01-0.07%. Further, we find that this modest amount of additional Sairdrone USV
934 sampling increases the global and Southern Ocean air-sea CO₂ flux by up to 0.1 Pg C yr⁻¹, a
935 quantity equivalent to 25 % of the uncertainty in the ocean carbon sink (0.4 Pg C yr⁻¹;
936 Friedlingstein et al., 2023). Our findings are consistent with previous studies suggesting that
937 additional observations during southern hemisphere winter months and covering meridional
938 gradients can reduce uncertainties and biases in the reconstructions (Lenton et al., 2006; Monteiro
939 et al., 2010; Djeutchouang et al., 2022; Mackay et al., 2022). As opposed to other autonomous
940 platform approaches, Sairdrone USVs obtain in situ pCO₂ observations with uncertainties
941 equivalent to the highest-quality observations collected by research ships ($\pm 2 \mu\text{atm}$; Sabine et al.,
942 2020; Sutton et al., 2021), and can operate at a high speed so that the spatial extent and seasonal
943 cycle of meridional gradients can be covered. The approach of combining high-accuracy Sairdrone
944 USV and SOCAT observations represents thus a promising solution to improve future surface

Deleted: The results from this experiment show

Deleted: 14

Deleted: 2

Deleted: 4

949 ocean pCO₂ reconstructions and the accuracy of the ocean carbon sink. Lastly, we show that the
950 large variability in bias, and the weakening of the global and Southern Ocean carbon sink in the
951 2000s, may be partially an artefact of Southern Ocean undersampling.

952 **Code availability**

953 Data analysis scripts will be made available in a GitHub repository upon publication.

954 **Data availability**

955 The Large Ensemble Testbed is publicly available at
956 https://figshare.com/collections/Large_ensemble_pCO2_testbed/4568555.

957

958 **Author contribution**

959 THH, GAM and AJS designed the experiments, and THH performed the simulations. THH, ARF
960 and LG developed the code. THH and ARF calculated the air-sea fluxes. THH prepared the
961 manuscript with contributions from all co-authors.

962 **Competing interests**

963 The authors declare that they have no conflict of interest.

964 **Acknowledgements**

965 We acknowledge funding from NOAA through the Climate Observations and Monitoring Program
966 (Award #NA20OAR4310340) and from NSF through the LEAP STC (Award #2019625). This is
967 PMEL contribution 5549. We would also like to acknowledge and thank Val Bennington, Julius
968 Busecke, Devan Samant and Abby Shaum for providing technical support, and Viviana Acquaviva
969 for discussions regarding the manuscript. Lastly, we wish to thank two anonymous reviewers,
970 whose contributions greatly improved the manuscript.

971

972 **References**

973

Deleted: and

Deleted:

Formatted: Font: 12 pt

Deleted:

977 Bakker, D. C. E., Pfeil, B., Landa, C. S., Metzl, N., O'Brien, K. M., Olsen, A., Smith, K., Cosca,
978 C., Harasawa, S., Jones, S. D., Nakaoka, S., Nojiri, Y., Schuster, U., Steinhoff, T., Sweeney, C.,
979 Takahashi, T., Tilbrook, B., Wada, C., Wanninkhof, R., Alin, S. R., Balestrini, C. F., Barbero, L.,
980 Bates, N. R., Bianchi, A. A., Bonou, F., Boutin, J., Bozec, Y., Burger, E. F., Cai, W.-J., Castle, R.
981 D., Chen, L., Chierici, M., Currie, K., Evans, W., Featherstone, C., Feely, R. A., Fransson, A.,
982 Goyet, C., Greenwood, N., Gregor, L., Hankin, S., Hardman-Mountford, N. J., Harlay, J., Hauck,
983 J., Hoppema, M., Humphreys, M. P., Hunt, C. W., Huss, B., Ibáñez, J. S. P., Johannessen, T.,
984 Keeling, R., Kitidis, V., Körtzinger, A., Kozyr, A., Krasakopoulou, E., Kuwata, A., Landschützer,
985 P., Lauvset, S. K., Lefèvre, N., Lo Monaco, C., Manke, A., Mathis, J. T., Merlivat, L., Millero, F.
986 J., Monteiro, P. M. S., Munro, D. R., Murata, A., Newberger, T., Omar, A. M., Ono, T., Paterson,
987 K., Pearce, D., Pierrot, D., Robbins, L. L., Saito, S., Salisbury, J., Schlitzer, R., Schneider, B.,
988 Schweitzer, R., Sieger, R., Skjelvan, I., Sullivan, K. F., Sutherland, S. C., Sutton, A. J., Tadokoro,
989 K., Telszewski, M., Tuma, M., van Heuven, S. M. A. C., Vandemark, D., Ward, B., Watson, A.
990 J., and Xu, S.: A multi-decade record of high-quality $f\text{CO}_2$ data in version 3 of the Surface Ocean
991 CO_2 Atlas (SOCAT), Earth System Science Data, 8, 383–413, [https://doi.org/10.5194/essd-8-383-](https://doi.org/10.5194/essd-8-383-2016)
992 [2016](https://doi.org/10.5194/essd-8-383-2016), 2016.

993 Bakker, D. C. E., Alin, S. R., Becker, M., Bittig, H. C., Castaño-Primo, R., Feely, R. A., Gkritzalis,
994 T., Kadono, K., Kozyr, A., Lauvset, S. K., Metzl, N., Munro, D. R., Nakaoka, S., Nojiri, Y., O'Brien,
995 K. M., Olsen, A., Pfeil, Benjamin, P., Denis, S., Tobias, S., Kevin F., Sutton, A. J., Sweeney, C.,
996 Tilbrook, B., Wada, C., Wanninkhof, R., Willstrand W. A., Akl, J., Apelthun, L. B., Bates, N.,
997 Beatty, C. M., Burger, E. F., Cai, W., Cosca, C. E., Corredor, J. E., Cronin, M., Cross, J. N., De
998 Carlo, E. H., DeGrandpre, M. D., Emerson, S. R., Enright, M. P., Enyo, K., Evans, W., Frangoulis,
999 C., Fransson, A., García-Ibáñez, M. I., Gehrung, M., Giannoudi, L., Glockzin, M., Hales, B.,
1000 Howden, S. D., Hunt, C. W., Ibáñez, J. S. P., Jones, S. D., Kamb, L., Körtzinger, A., Landa, C.
1001 S., Landschützer, P., Lefèvre, N., Lo Monaco, C., Macovei, V. A., Maenner J. S., Meinig, C.,
1002 Millero, F. J., Monacci, N. M., Mordy, C., Morell, J. M., Murata, A., Musielewicz, S., Neill, .,
1003 Newberger, T., Nomura, D., Ohman, M., Ono, T., Passmore, A., Petersen, W., Petihakis, G.,
1004 Perivoliotis, L., Plueddemann, A. J., Rehder, G., Reynaud, T., Rodriguez, C., Ross, A. C.,
1005 Rutgersson, A., Sabine, C. L., Salisbury, J. E., Schlitzer, R., Send, U., Skjelvan, I., Stamataki, N.,
1006 Sutherland, S. C., Sweeney, C., Tadokoro, K., Tanhua, T., Telszewski, M., Trull, T., Vandemark,
1007 D., van Ooijen, E., Voynova, Y. G., Wang, H., Weller, R. A., Whitehead, C., Wilson, D.: Surface

1008 Ocean CO₂ Atlas Database Version 2022 (SOCATv2022) (NCEI Accession 0253659), NOAA
1009 National Centers for Environmental Information [dataset], <https://doi.org/10.25921/1h9f-nb73>,
1010 2022.

1011 [Behncke, J., Landschützer, P. & Tanhua, T. A detectable change in the air-sea CO₂ flux estimate
1012 from sailboat measurements. *Scientific Reports*, 14, 3345, \[https://doi.org/10.1038/s41598-024-
53159-0\]\(https://doi.org/10.1038/s41598-024-
1013 53159-0\), 2024.](#)

1014 Bennington, V., Galjanic, T., and McKinley, G. A.: Explicit Physical Knowledge in Machine
1015 Learning for Ocean Carbon Flux Reconstruction: The pCO₂-Residual Method, Journal of
1016 Advances in Modeling Earth Systems, 14(10), <https://doi.org/10.1029/2021ms002960>, 2022a.

1017 Bennington, V., Gloege, L., and McKinley, G. A.: Variability in the global ocean carbon sink from
1018 1959 to 2020 by correcting models with observations, Geophysical Research Letters, 49(14),
1019 <https://doi.org/10.1029/2022GL098632>, (2022b).

1020 Bushinsky, S. M., Landschützer, P., Rödenbeck, C., Gray, A. R., Baker, D., Mazloff, M. R.,
1021 Resplandy, L., Johnson, K. S., and Sarmiento, J. L.: Reassessing Southern Ocean air-sea CO₂ flux
1022 estimates with the addition of biogeochemical float observations, Global Biogeochemical Cycles,
1023 33(11), 1370-1388, <https://doi.org/10.1029/2019GB006176>, 2019.

1024 Chen, T., and Guestrin, C.: Xgboost: A scalable tree boosting system, In: Proceedings of the 22nd
1025 ACM SIGKDD international conference on knowledge discovery and data mining (pp. 785-794),
1026 <https://doi.org/10.1145/2939672.2939785>, 2016.

1027 [Denvil-Sommer, A., Gehlen, M., and Vrac, M.: Observation system simulation experiments in the
1028 Atlantic Ocean for enhanced surface ocean pCO₂ reconstructions. *Ocean Science*, 17, 1011-1030,
1029 <https://doi.org/10.5194/os-17-1011-2021>, 2021.](#)

1030 Deser, C., Phillips, A., Bourdette, V., and Teng, H.: Uncertainty in climate change projections: the
1031 role of internal variability, Climate Dynamics, 38, 527-546, [https://doi.org/10.1007/s00382-010-
0977-x](https://doi.org/10.1007/s00382-010-
1032 0977-x), 2012

1033 Djeutchouang, L. M., Chang, N., Gregor, L., Vichi, M., and Monteiro, P. M. S.: The sensitivity of
1034 pCO₂ reconstructions to sampling scales across a Southern Ocean sub-domain: a semi-idealized

Formatted: Font: (Default) Times New Roman, 12 pt

Formatted: Font: (Default) Times New Roman, 12 pt, Not Bold

Formatted: Font: (Default) Times New Roman, 12 pt

Formatted: Font: (Default) Times New Roman, 12 pt

Field Code Changed

Deleted: ¶

Formatted: Font color: Text 1

Formatted: Subscript

Formatted: Font: Italic

Formatted: Hyperlink, Font: (Default) Times New Roman, 12 pt, Font color: Auto, Pattern: Clear

Field Code Changed

1036 ocean sampling simulation approach, *Biogeosciences*, 19, 4171-4195, [https://doi.org/10.5194/bg-](https://doi.org/10.5194/bg-19-4171-2022)
1037 [19-4171-2022](https://doi.org/10.5194/bg-19-4171-2022), 2022

1038 Fay, A. R., Lovenduski, N. S., McKinley, G. A., Munro, D. R., Sweeney, C., Gray, A. R.,
1039 Landschützer, P., Stephens, B. B., Takahashi, T., and Williams, N.: Utilizing the Drake Passage
1040 Time-series to understand variability and change in subpolar Southern Ocean pCO₂,
1041 *Biogeosciences*, 15(12), 3841-3855, <https://doi.org/10.5194/bg-15-3841-2018>, 2018.

1042 Fay, A. R., and McKinley, G. A.: Observed regional fluxes to constrain modeled estimates of the
1043 ocean carbon sink, *Geophysical Research Letters*, 48(20), <https://doi.org/10.1029/2021GL095325>,
1044 2021.

1045
1046 [Friedlingstein, P., O'Sullivan, M., Jones, M. W., Andrew, R. M., Bakker, D. C. E., Hauck, J.,](#)
1047 [Landschützer, P., Le Quéré, C., Luijkx, I. T., Peters, G. P., Peters, W., Pongratz, J., Schwingshackl,](#)
1048 [C., Sitch, S., Canadell, J. G., Ciais, P., Jackson, R. B., Alin, S. R., Anthoni, P., Barbero, L., Bates,](#)
1049 [N. R., Becker, M., Bellouin, N., Decharme, B., Bopp, L., Brasika, I. B. M., Cadule, P.,](#)
1050 [Chamberlain, M. A., Chandra, N., Chau, T.-T., Chevallier, F., Chini, L. P., Cronin, M., Dou,](#)
1051 [X., Enyo, K., Evans, W., Falk, S., Feely, R. A., Feng, L., Ford, D. J., Gasser, T., Ghattas, J.,](#)
1052 [Gkritzalis, T., Grassi, G., Gregor, L., Gruber, N., Gürses, Ö., Harris, I., Hefner, M., Heinke, J.,](#)
1053 [Houghton, R. A., Hurtt, G. C., Iida, Y., Ilyina, T., Jacobson, A. R., Jain, A., Jarníková, T., Jersild,](#)
1054 [A., Jiang, F., Jin, Z., Joos, F., Kato, E., Keeling, R. F., Kennedy, D., Klein Goldewijk, K., Knauer,](#)
1055 [J., Korsbakken, J. I., Körtzinger, A., Lan, X., Lefèvre, N., Li, H., Liu, J., Liu, Z., Ma, L., Marland,](#)
1056 [G., Mayot, N., McGuire, P. C., McKinley, G. A., Meyer, G., Morgan, E. J., Munro, D. R., Nakaoka,](#)
1057 [S.-I., Niwa, Y., O'Brien, K. M., Olsen, A., Omar, A. M., Ono, T., Paulsen, M., Pierrot, D., Pockock,](#)
1058 [K., Poulter, B., Powis, C. M., Rehder, G., Resplandy, L., Robertson, E., Rödenbeck, C., Rosan, T.,](#)
1059 [M., Schwinger, J., Séférian, R., Smallman, T. L., Smith, S. M., Sospedra-Alfonso, R., Sun, Q.,](#)
1060 [Sutton, A. J., Sweeney, C., Takao, S., Tans, P. P., Tian, H., Tilbrook, B., Tsujino, H., Tubiello, F.,](#)
1061 [van der Werf, G. R., van Ooijen, E., Wanninkhof, R., Watanabe, M., Wimart-Rousseau, C., Yang,](#)
1062 [D., Yang, X., Yuan, W., Yue, X., Zaehle, S., Zeng, J., and Zheng, B.: Global Carbon Budget 2023,](#)
1063 [Earth Syst. Sci. Data](#), 15, 5301–5369, <https://doi.org/10.5194/essd-15-5301-2023>, 2023.

Formatted: Font: (Default) Times New Roman, 12 pt

1064 Fyfe, J. C., Derksen, C., Mudryk, L., Flato, G. M., Santer, B. D., Swart, N. C., Molotch, N. P.,
1065 Zhang, X., Wan, H., Arora, V. K., Scinocca, J., and Jiao, Y.: Large near-term projected snowpack
1066 loss over the western United States, *Nature communications*, 8(1), 14996,
1067 <https://doi.org/10.1038/ncomms14996>, 2017.

1068 Gloege, L., McKinley, G. A., Landschützer, P., Fay, A. R., Frolicher, T. L., and Fyfe, J. C.:
1069 Quantifying Errors in Observationally Based Estimates of Ocean Carbon Sink Variability, *Global*
1070 *Biogeochemical Cycles*, 35(4), <https://doi.org/10.1029/2020gb006788>, 2021.

1071 Gloege, L., Yan, M., Zheng, T. and McKinley, G. A.: Improved quantification of ocean carbon
1072 uptake by using machine learning to merge global models and pCO₂ data, *Journal of Advances in*
1073 *Modeling Earth Systems*, 14(2), <https://doi.org/10.1029/2021MS002620>, 2022.

1074

1075 Good, S. A., Martin, M., and Rayner, N. A.: EN4: Quality controlled ocean temperature and
1076 salinity profiles and monthly objective analyses with uncertainty estimates, *Journal of*
1077 *Geophysical Research Oceans*, 118(12), 6704-6717, <https://doi.org/10.1002/2013JC009067>,
1078 2013.

1079

1080 Gray, A. R., Johnson, K. S., Bushinsky, S. M., Riser, S. C., Russell, J. L., Talley, L. D.,
1081 Wanninkhof, R., Williams, N. L., and Sarmiento, J. L.: Autonomous biogeochemical floats detect
1082 significant carbon dioxide outgassing in the high-latitude Southern Ocean, *Geophysical Research*
1083 *Letters*, 45(17), 9049-9057, <https://doi.org/10.1029/2018GL078013>, 2018.

1084 Gregor, L., Lebehot, A. D., Kok, S., and Monteiro, P. M. S.: A comparative assessment of the
1085 uncertainties of global surface ocean CO₂ estimates using a machine-learning ensemble (CSIR-
1086 ML6 version 2019a) – have we hit the wall?, *Geoscientific Model Development*, 12, 5113-5136,
1087 <https://doi.org/10.5194/gmd-12-5113-2019>, 2019.

1088 Gregor, L. and Fay, A. R.: Air-sea CO₂ fluxes for surface pCO₂ data products using a standardized
1089 approach, Zenodo [code], <https://doi.org/10.5281/zenodo.5482547>, 2021.

1090 Gruber, N., Landschützer, P., and Lovenduski, N. S.: The variable Southern Ocean carbon sink,
1091 *The Annual Review of Marine Science*, 11, 159-86, [https://doi.org/10.1146/annurev-marine-](https://doi.org/10.1146/annurev-marine-121916-063407)
1092 [121916-063407](https://doi.org/10.1146/annurev-marine-121916-063407), 2019.

Deleted: Friedlingstein, P., Jones, M. W., O'Sullivan, M., Andrew, R. M., Bakker, D. C., Hauck, J., Le Quéré, C., Peters, G. P., Peters, W., Pongratz, J., Sitch, S., Canadell, J. G., Ciais, P., Jackson, R. B., Alin, S. R., Anthoni, P., Bates, N. R., Becker, M., Bellouin, N., Bopp, L., Chau, T. T. T., Chevallier, F., Chini, L. P., Cronin, M., Currie, K. I., Decharme, B., Djeutchouang, L., Dou, X., Evans, W., Feely, R. A., Feng, L., Gasser, T., Gilfillan, D., Gkritzalis, T., Grassi, G., Gregor, L., Gruber, N., Gürses, Ö., Harris, I., Houghton, R. A., Hurtt, C. C., Iida, Y., Ilyina, T., Luijckx, I. T., Jain, A. K., Jones, S. D., Kato, E., Kennedy, D., Goldewijk, K. K., Knauer, J., Korsbakken, J. A., Körtzinger, A., Landschützer, P., Lauvset, S. K., Lefèvre, N., Lienert, S., Liu, J., Marland, G., McGuire, P. C., Melton, J. R., Munro, D. R., Nabel, J. E. M. S., Nakaoka, S.-I., Niwa, Y., Ono, T., Pierrot, D., Poulter, B., Rehder, G., Resplandy, L., Robertson, E., Rödenbeck, C., Rosan, T. M., Schwingler, J., Schwingshackl, C., Séférian, R., Sutton, A. J., Sweeney, C., Tanhua, T., Tans, P. P., Tian, H., Tilbrook, B., Tubiello, F., Werf, G. V. D., Vuichard, N., Wada, C., Wanninkhof, R., Watson, A., Willis, D., Wiltshire, A. J., Yuan, W., Yue, C., Yue, X., Zaehle, S., and Zeng, J.: Global carbon budget 2021, *Earth System Science Data*, 14(4), 1917-2005, <https://doi.org/10.5194/essd-14-1917-2022>, 2022

1117 [Hauck, J., Nissen, C., Landschützer, P., Rödenbeck, C., Bushinsky, S., and Olsen, A.: Sparse](#)
1118 [observations induce large biases in estimates of the global ocean CO₂ sink: and ocean model](#)
1119 [subsampling experiment, Philosophical Transactions Of the Royal Society A, 381:20220063,](#)
1120 <https://doi.org/10.1098/rsta.2022.0063>, 2023.

Formatted: Font: 12 pt

Formatted: Font: 12 pt

1121 Kay, J. E., Deser, C., Phillips, A., Mai, A., Hannay, C., Strand, G., Arblaster, J. M., Bates, S. C.,
1122 Danabasoglu, G., Edwards, J., Holland, M., Kuschner, P., Lamarque, J-F., Lawrence, D., Lindsay,
1123 K., Middelton, A., Munoz, E., Neale, R., Oleson, K., Polvani, L., and Vertenstein, M.: The
1124 Community Earth System Model (CESM) large ensemble project: A community resource for
1125 studying climate change in the presence of internal climate variability, *Bulletin of the American*
1126 *Meteorological Society*, 96(8), 1333-1349, <https://doi.org/10.1175/BAMS-D-13-00255>, 2015.

1127 Khatiwala, S., Primeau, F., and Hall, T.: Reconstruction of the history of anthropogenic CO₂
1128 concentrations in the ocean, *Nature*, 462(7271), 346-349, <https://doi.org/10.1038/nature08526>,
1129 2009.

1130 Landschützer, P., Gruber, N., Bakker, D. C. E., and Schuster, U.: Recent variability of the global
1131 ocean carbon sink, *Global Biogeochemical Cycles*, 28(9), 927-949,
1132 <https://doi.org/10.1002/2014GB004853>, 2014.

1133 Landschützer, P., Gruber, N., Haumann, F. A., Rödenbeck, C., Bakker, D. C. E., Van Heuven, S.,
1134 Hoppema, M., Metzl, N., Sweeney, C., Takahashi, T., Brook, B., and Wanninkhof, R.: The
1135 reinvigoration of the Southern Ocean carbon sink, *Science*, 349(6253), 1221-1224,
1136 <https://doi.org/10.1126/science.aab2620>, 2015.

Deleted: .

1137 Landschützer, P., Tanhua, T., Behncke, J., and Keppler, L.: Sailing through the Southern Ocean
1138 seas of air-sea CO₂ flux uncertainty, *Philosophical Transactions of the Royal Society A*, 381,
1139 <https://doi.org/10.1098/rsta.2022.0064>, 2023.

1140 Lenton, A. B., Matear, R. J., and Tilbrook, B.: Design of an observational strategy for quantifying
1141 the Southern Ocean uptake of CO₂, *Global Biogeochemical Cycles*, 20, 1-11.
1142 <https://doi.org/10.1029/2005GB002620>, 2006.

1143 Lenton, A. B., Tilbrook, B., Law, R. M., Bakker, D. C. E., Doney, S. C., Gruber, N., Ishii, M.,
1144 Hoppema, M., Lovenduski, N. S., Matear, R. J., McNeil, B. I., Metzl, N., Mikaloff Fletcher, S. E.,

1146 Monteiro, P. M. S., Rödenbeck, C., Sweeney, C., and Takahashi, T.: Sea-air CO₂ fluxes in the
1147 Southern Ocean for the period 1990-2009, *Biogeosciences*, 10, 4037-4054,
1148 <https://doi.org/10.5194/bg-10-4037-2013>, 2013.

1149 Le Quéré, C., Rödenbeck, C., Buitenhuis, E. T., Conway, T. J., Lagenfelds, R., Gomez, A.,
1150 Labuschagne C., Ramonet, M., Nakazawa, T., Metzl, N., Gillett, N., and Heimann, M.: Saturation
1151 of the Southern Ocean CO₂ sink due to recent climate change, *Science*, 316(5832), 1735-1738,
1152 <https://doi.org/10.1126/science.1136188>, 2007.

1153 Long, M. C., Stephens, B. B., McKain, K., Sweeney, C., Keeling, R. F., Kort, E. A., Morgan, E.
1154 J., Bent, J. D., Chandra, N., Chevallier, F., Commane, R., Daube, B. C., Krummel, P. B., Loh, Z.,
1155 Luijkx, I. T., Munro, D., Patra, P., Peters, W., Ramonet, M., Rödenbeck, C., Stavert, A., Tans, P.,
1156 and Wofsy, S. C.: Strong Southern Ocean carbon uptake evident in airborne observations, *Science*,
1157 374(6572), 1275-1280, <https://doi.org/10.1126/science.abi4355>, 2021.

1158 Mackay, N., and Watson, A.: Winter air-sea CO₂ fluxes constructed from summer observations of
1159 the polar Southern Ocean suggest weak outgassing, *Journal of Geophysical Research: Oceans*,
1160 126(5), e2020JC016600, <https://doi.org/10.1029/2020JC016600>, 2021.

1161 Mackay, N., Watson, A., Suntharalingam, P., Chen, Z., and Rödenbeck, C.: Improved winter data
1162 coverage of the Southern Ocean CO₂ sink from extrapolation of summertime observations,
1163 *Communications Earth & Environment*, 3, 265, <https://doi.org/10.1038/s43247-022-00592-6>,
1164 2022.

1165 McKinley, G. A., Fay, A. R., Eddebbar, Y. A., Gloege, L., and Lovenduski, N. S.: External forcing
1166 explains recent decadal variability of the ocean carbon sink, *AGU Advances*, 1(2),
1167 e2019AV000149, <https://doi.org/10.1029/2019AV000149>, 2020.

1168 Mongwe, N. P., Vichi, M., and Monteiro, P. M. S.: The seasonal cycle of *p*CO₂ and CO₂ fluxes in
1169 the Southern Ocean: diagnosing anomalies in CMIP5 Earth system models, *Biogeosciences*, 15(9),
1170 2851-2872, <https://doi.org/10.5194/bg-15-2851-2018>, 2018.

1171 Monteiro, P. M. S., Gregor, L., Lévy, M., Maenner, S., Sabine, C. L., and Swart, S.: Intraseasonal
1172 variability linked to sampling alias in air-sea CO₂ fluxes in the Southern Ocean, *Geophysical*
1173 *Research Letters*, 42(20), 8507-8514, <https://doi.org/10.1002/2015GL066009>, 2015.

1174 Rodgers, K. B., Lin, J., and Frölicher, T. L.: Emergence of multiple ocean ecosystem drivers in a
1175 large ensemble suite with an Earth system model, *Biogeosciences*, 12(11), 3301-3320.
1176 <https://doi.org/10.5194/bg-12-3301-2015>, 2015.

1177 Rödenbeck, C., Bakker, D. C. E., Gruber, N., Iida, Y., Jacobson, A. R., Jones, S., Landschützer,
1178 P., Metzl, N., Nakaoka, S., Olsen, A., Park, G.-H., Peylin, P., Rodgers, K. B., Sasse T. P., Schuster,
1179 U., Shutler, J. D., Valsala, V., Wanninkhof, R., and Zeng, J.: Data-based estimates of the ocean
1180 carbon sink variability – first results of the Surface Ocean $p\text{CO}_2$ Mapping intercomparison
1181 (SOCOM), *Biogeosciences*, 12, 7251-7278, <https://doi.org/10.5194/bg-12-7251-2015>, 2015.

1182 Sabine, C., Sutton, A., McCabe, K., Lawrence-Slavas, N., Alin, S, Feely, R., Jenkins, R., Maenner,
1183 S., Meinig, C., Thomas, J., van Ooijen, E., Passmore, A., and Tilbrook, B.: Evaluation of a new
1184 carbon dioxide system for autonomous surface vehicles, *Journal of Atmospheric and Oceanic*
1185 *Technology*, 37(8), 1305-1317, <https://doi.org/10.1175/JTECH-D-20-0010.1>, 2020.

1186 Stamell, J., Rustagi, R. R., Gloege, L., and McKinley, G. A.: Strengths and weaknesses of three
1187 Machine Learning methods for $p\text{CO}_2$ interpolation, *Geoscientific Model Development*
1188 *Discussions*[preprint], doi:10.5194/gmd-2020-311, 22 October 2020.

1189 Sutton, A. J., Williams, N. L., and Tilbrook, B.: Constraining Southern Ocean CO_2 flux uncertainty
1190 using uncrewed surface vehicle observations, *Geophysical Research Letters*, 48(3),
1191 e2020GL091748, <https://doi.org/10.1029/2020GL091748>, 2021.

1192 Takahashi, T., Olafsson, J., Goddard, J. G., Chipman, D. W., and Sutherland, S. C.: Seasonal
1193 variation of CO_2 and nutrients in the high-latitude surface oceans: A comparative study, *Global*
1194 *Biogeochemical Cycles*, 7(4), 843-878, <https://doi.org/10.1029/93GB02263>, 1993.

1195 Takahashi, T., Sutherland, S. C., Wanninkhof, R., Sweeney, C., Feely, R. A., Chipman, D. W.,
1196 Hales, B., Friederich, G., Chavez, F., Sabine, C., Watson, A., Bakker, D. C. E., Schuster, U., Metzl,
1197 N., Yoshikawa-Inoue, H., Ishii, M., Midorikawa, T., Nojiri, Y., Körtzinger, A., Steinhoff, T.,
1198 Hoppema, M., Olafsson, J., Arnarson, T. S., Tilbrook, B., Johannessen, T., Olsen, A., Bellerby,
1199 R., Wong, C. S., Delille, B., Bates, N. R., and de Baar, H. J. W.: Climatological mean and decadal
1200 change in surface ocean $p\text{CO}_2$, and net sea-air CO_2 flux over the global oceans, *Deep Sea Research*

Deleted: .

Deleted: ¶

1203 Part II: Topical Studies in Oceanography, 56(8-10), 554-557,
1204 <https://doi.org/10.1016/j.dsr2.2008.12.009>, 2009.

1205 Toms, B. A., Barnes, E. A., and Ebert-Uphoff, I.: Physically interpretable neural networks for the
1206 geosciences: Applications to earth system variability, *Journal of Advances in Modeling Earth*
1207 *Systems*, 12(9), e2019MS002002, <https://doi.org/10.1029/2019MS002002>, 2020.

1208 Williams, N. L., Juranek, L. W., Feely, R. A., Johnson, K. S., Sarmiento, J. L., Talley, L. D.,
1209 Dickson, A. G., Gray, A. R., Wannikhof, R., Russell, J. L., Riser, S. C., and Takeshita, Y.:
1210 Calculating surface ocean pCO₂ from biogeochemical Argo floats equipped with pH: An
1211 uncertainty analysis, *Global Biogeochemical Cycles*, 31(3), 591-604,
1212 <https://doi.org/10.1002/2016GB005541>, 2017.

1213 Wu, Y., Bakker, D. C. E., Achterberg, E. P., Silva, A. N., Pickup D. P., Li, X., Hartman, S.,
1214 Stappard, D., Qi, D., and Tyrrell, T.: Integrated analysis of carbon dioxide and oxygen
1215 concentrations as a quality control of ocean float data, *Communications Earth & Environment*, 3,
1216 92, <https://doi.org/10.1038/s43247-022-00421-w>, 2022.

1217

1218

1219

1220

1221

1222

Page 18: [1] Deleted Thea Hatlen Heimdal 12/14/23 4:52:00 PM

▼ ◀
▲

Page 18: [1] Deleted Thea Hatlen Heimdal 12/14/23 4:52:00 PM

▼ ◀
▲

Page 18: [1] Deleted Thea Hatlen Heimdal 12/14/23 4:52:00 PM

▼ ◀
▲

Page 18: [1] Deleted Thea Hatlen Heimdal 12/14/23 4:52:00 PM

▼ ◀
▲

Page 18: [1] Deleted Thea Hatlen Heimdal 12/14/23 4:52:00 PM

▼ ◀
▲

Page 18: [1] Deleted Thea Hatlen Heimdal 12/14/23 4:52:00 PM

▼ ◀
▲

Page 18: [1] Deleted Thea Hatlen Heimdal 12/14/23 4:52:00 PM

▼ ◀
▲

Page 18: [1] Deleted Thea Hatlen Heimdal 12/14/23 4:52:00 PM

▼ ◀
▲

Page 18: [1] Deleted Thea Hatlen Heimdal 12/14/23 4:52:00 PM

▼ ◀
▲

Page 18: [1] Deleted Thea Hatlen Heimdal 12/14/23 4:52:00 PM

▼ ◀
▲

Page 18: [1] Deleted Thea Hatlen Heimdal 12/14/23 4:52:00 PM

▼ ◀
▲

Page 22: [2] Deleted Thea Hatlen Heimdal 11/27/23 2:39:00 PM

▼ ◀

▲.....
Page 22: [2] Deleted Thea Hatlen Heimdal 11/27/23 2:39:00 PM

▼.....
Page 22: [2] Deleted Thea Hatlen Heimdal 11/27/23 2:39:00 PM

▼.....
Page 22: [2] Deleted Thea Hatlen Heimdal 11/27/23 2:39:00 PM

▼.....
Page 22: [2] Deleted Thea Hatlen Heimdal 11/27/23 2:39:00 PM

▼.....
Page 22: [2] Deleted Thea Hatlen Heimdal 11/27/23 2:39:00 PM

▼.....
Page 22: [2] Deleted Thea Hatlen Heimdal 11/27/23 2:39:00 PM

▼.....
Page 22: [2] Deleted Thea Hatlen Heimdal 11/27/23 2:39:00 PM

▼.....
Page 22: [2] Deleted Thea Hatlen Heimdal 11/27/23 2:39:00 PM

▼.....
Page 22: [2] Deleted Thea Hatlen Heimdal 11/27/23 2:39:00 PM

▼.....
▲.....